

Numerical modelling of bulk viscosity in neutron stars

Michail Chabanov^{1,2,*} and Luciano Rezzolla^{1,3,4}

¹*Institut für Theoretische Physik, Goethe Universität, Max-von-Laue-Str. 1, 60438 Frankfurt am Main, Germany*

²*Center for Computational Relativity and Gravitation & School of Mathematical Sciences,*

Rochester Institute of Technology, 85 Lomb Memorial Drive, Rochester, New York 14623, USA

³*Frankfurt Institute for Advanced Studies, Ruth-Moufang-Str. 1, 60438 Frankfurt am Main, Germany*

⁴*School of Mathematics, Trinity College, Dublin 2, Ireland*

(Dated: March 6, 2025)

The early post-merger phase of a binary neutron-star coalescence is shaped by characteristic rotational velocities as well as violent density oscillations and offers the possibility to constrain the properties of neutron star matter by observing the gravitational wave emission. One possibility to do so is the investigation of gravitational wave damping through the bulk viscosity which originates from violations of weak chemical equilibrium. Motivated by these prospects, we present a comprehensive report about the implementation of the self-consistent and second-order formulation of the equations of relativistic hydrodynamics for dissipative fluids proposed by Müller, Israel and Stewart. Furthermore, we report on the results of two test problems, namely the viscous damping of linear density oscillations of isolated nonrotating neutron stars and the viscous migration test, both of which confirm our implementation and can be used for future code tests. Finally, we present fully general-relativistic simulations of viscous binary neutron-star mergers. We explore the structural and thermal properties of binary neutron-star mergers with a constant bulk-viscosity prescription and investigate the impact of bulk viscosity on dynamical mass ejection. We find that inverse Reynolds numbers $\sim 1\%$ can be achieved for the highest employed viscosity thereby suppressing the dynamically ejected mass by a factor of ~ 5 compared to the inviscid case.

I. INTRODUCTION

Binary neutron star mergers (BNSs) are extremely violent and nonlinear phenomena in which all of the four fundamental interactions play an important role. This makes them ideal multi-messenger astronomical observables which harbour the potential to place constraints on gravity or the strong interaction of dense matter in regimes otherwise not accessible by terrestrial experiments. For example, the first multi-messenger detection of a BNS merger, GW170817 [1–3], provided constraints on the properties of isolated nonrotating neutron stars, e.g., their maximum mass M_{TOV} or their distribution in radii [4–14], which can be directly used to narrow the band of allowed equations of state (EOS) of cold nuclear matter. The acronym TOV stands for Tolman-Oppenheimer-Volkoff. Many of these results stem solely from the inspiral gravitational-wave (GW) signal, the post-merger signal, however, will offer even more information about the EOS at extreme densities [15–20], in particular when the possible appearance of a phase transition to quark matter is invoked [21–30].

Another promising avenue to infer the EOS of dense matter through the post-merger GW signal constitutes possible imprints of microphysical transport effects, such as bulk viscosity, which lead to damped GW emission. Bulk viscosity can emerge effectively through violations of weak chemical equilibrium and results from the out-of-equilibrium dynamics that accompanies the post-merger remnant in the first few milliseconds since its formation [31–37] (see [38, 39] for some recent work on the inspiral).

By considering URCA processes involving npe or $npe\mu$ matter several studies estimated post-merger kHz-density oscillations to be damped over a timescale $\lesssim 100$ ms after the merger [40–43]. In addition, it was shown in a recent investigation exploring the impact of npe URCA processes in BNS simulations that the bulk-viscous approximation is valid in large parts of the hypermassive neutron star (HMNS) [44]. Furthermore, results from moment-based treatments of neutrino transport have not found evidence for large out-of-thermodynamic equilibrium effects as those needed to produce an effective bulk viscosity [45], although being present in the first few milliseconds after the merger [46].

In our recent work [47], we obtain the first quantitatively robust assessment of the impact of bulk viscosity on the post-merger GW signal from BNS mergers by using the causal and second-order formulation of dissipative hydrodynamics by Müller, Israel and Stewart (MIS) [48–55] (see also [56] for preliminary studies in spherical symmetry and [57–61] for other interesting approaches to viscous dissipation in general-relativistic simulations). Our microphysical description consists of a bulk viscosity that is determined by direct and modified Urca reactions that are responsible for achieving weak chemical equilibrium in neutron-star matter. In addition, we vary the composition of cold neutron-star matter above the nuclear-saturation density in order to study systematically the impact of small (realistic) and large (unrealistic) bulk viscosities. These scenarios can be seen as corresponding to four different resonant maxima of the so-called “AC bulk viscosity” [62] $\zeta_{\text{AC}}(\omega) := \zeta(1 + \omega^2\tau_{\text{n}}^2)^{-1}$, where ζ , τ_{n} and ω denote respectively the bulk viscosity, the relaxation time and the angular frequency of a periodic density oscillation [63, 64].

We find that large bulk viscosities are effective at damping the collision-and-bounce oscillations of the stellar cores while, at the same time, preserving the initial $m = 2$ density

* micsma@rit.edu

deformations of the binary. The main consequences of the increase of the bar-mode deformations constitute, on one hand, an increase of the efficiency of energy and angular-momentum losses via GWs. On the other hand, the stellar structure of the HMNS is modified and is characterised by a more compact remnant with uniformly rotating core spinning faster than in the inviscid case but having the same rotational kinetic energy. The larger spinning frequency of the viscous remnants is reflected in a larger value for the f_2 frequency in the post-merger power spectral density (PSD). While the behaviour described above applies to all viscous binaries, the differences between viscous and inviscid binaries become significant only for the most extreme configurations.

This paper presents a comprehensive report on the numerical methods applied in [47] where, however, we make use of a particularly simplified microphysical model for the bulk viscosity. More specifically, we here assume a *constant* value within the neutron stars which is set to zero below a certain threshold density. Differently from our investigation in [47], where the transport coefficients arise consistently from microphysical arguments leading to complex functions of density and temperature, this is clearly an approximation. However, this treatment has the important advantage of being independent of the EOS and thus more suitable for serving as a numerical testbed.

We provide a detailed description of the algorithm solving the MIS equations for bulk viscosity with particular focus on various limiting procedures implemented in the inversion procedure from conservative to primitive variables in Section II. Then, we provide two test cases employing isolated neutron stars which are used to verify the implementation. First, in Subsection III A we simulate the viscous damping of density perturbations of TOV solutions and second, in Subsection III B we analyze the migration of TOV solutions from the unstable branch to the stable branch with bulk viscosity. The two test cases provide a qualitative and quantitative assessment of the implementation introduced before in Section II. Finally, in Subsection III C we present a detailed report on BNS simulations using a constant bulk viscosity within the stars where we report on thermal properties, density and temperature distributions as well as dynamical mass ejection. Last but not least, the conclusion of this work can be found in Section IV.

Unless stated otherwise, we use geometrised units where the speed of light $c = 1$ and the gravitational constant $G = 1$. Additionally, we set the Boltzmann constant $k_B = 1$ and express the temperature in units of MeV. Greek letters denote spacetime indices, i.e., $\mu = 0, 1, 2, 3$, while Roman letters cover spatial indices only, i.e., $i = 1, 2, 3$. Also, we make use of Einstein's summation convention and choose the metric signature to be $(-, +, +, +)$. Bold symbols, such as \mathbf{g} , refer to tensors of generic rank, while the symbol ∇ denotes the covariant derivative with respect to the four-metric \mathbf{g} .

II. FORMULATION AND METHODS

We solve the second-order MIS equations (see also [65–71] for recent progress on first-order theories) excluding the effects of heat conduction and shear viscosity. To do so, we follow closely the equations presented in [72] and refer to this work for a more detailed presentation and discussion of the mathematical formalism as well as the equations describing heat conduction and shear viscosity. We also evolve the space-time metric in order to explore self-consistently the effects of bulk viscosity in BNS merger simulations. In the following, we briefly summarize the evolved set of equations.

We start by introducing the 3+1 split of the metric [52, 73]

$$ds^2 = -(\alpha^2 - \beta_i \beta^i) dt^2 + 2\beta_i dx^i dt + \gamma_{ij} dx^i dx^j, \quad (1)$$

where α is the so-called lapse function, the purely spatial vector β^i is the shift vector, and γ_{ij} denotes the components of the purely spatial metric with $\gamma := \det(\gamma_{ij})$ defining its determinant. The fluid is described by the baryonic rest-mass density current and the energy-momentum tensor for a dissipative fluid with zero heat conduction and shear viscosity, i.e., only bulk viscosity, which in the Eckart frame are given by

$$J^\mu = \rho u^\mu \quad (2)$$

$$T^{\mu\nu} = e u^\mu u^\nu + (p + \Pi) h^{\mu\nu}, \quad (3)$$

respectively. The thermodynamic quantities ρ, e, p and Π denote the baryonic rest-mass density, the total energy density, the pressure in thermodynamic equilibrium and the bulk-viscous pressure, respectively. The bulk-viscous pressure can be understood as the correction to p arising from out-of-equilibrium effects. The vector $u^\mu = W(1/\alpha, v^i/\alpha - \beta^i/\alpha)^T$ denotes the fluid four-velocity where v^i are the components of the Eulerian three-velocity together with the Lorentz factor $W := \sqrt{1 - v_i v^i}^{-1}$. At this point we also define the “coordinate velocity” $V^j := u^j/u^t = \alpha v^j - \beta^j$. The conservation of baryon number as well as energy and momentum read

$$\nabla_\mu J^\mu = 0, \quad (4)$$

$$\nabla_\mu T^{\mu\nu} = 0, \quad (5)$$

respectively. Together with the choice of an EOS, i.e., $p = p(\rho, T)$, where T is the temperature of the fluid, we are left to specify a constitutive relation for Π in order to close the system of equations. As in [47, 72] we employ the Maxwell-Cattaneo model

$$\tau_\Pi u^\mu \nabla_\mu \Pi = \Pi_{\text{NS}} - \Pi, \quad (6)$$

$$\Pi_{\text{NS}} := -\zeta \Theta, \quad (7)$$

where $\mathbf{u} \cdot \nabla = u^\mu \nabla_\mu$ refers to the covariant derivative along the fluid four-velocity while Π_{NS} and $\Theta := \nabla_\mu u^\mu$ denote the so-called Navier-Stokes (NS) value and the fluid expansion, respectively. Further information on Eq. (6) can be found in [72]. It is interesting to note that recent work on the relation between chemically reacting multi-fluids and bulk-viscous single-fluids has shown that Eq. (6) can be used to

account even for the full out-of-equilibrium dynamics of a multi-fluid with two species [62, 74].

Altogether, we can write Eqs. (4), (5) and (6) in the flux-conservative form

$$\partial_t \mathbf{U} + \partial_i \mathbf{F}^i(\mathbf{U}) = \mathbf{S}(\mathbf{U}, \partial_\mu \mathbf{U}), \quad (8)$$

where \mathbf{U} , \mathbf{F}^i and \mathbf{S} denote the state, flux and source vectors, respectively. For Eqs. (4)-(6) their components are given by

$$\mathbf{U} := \sqrt{\gamma} \begin{pmatrix} D \\ S_j \\ \tau \\ D\Pi \end{pmatrix} = \sqrt{\gamma} \begin{pmatrix} \rho W \\ (e + p + \Pi) W^2 v_j \\ (e + p + \Pi) W^2 - (p + \Pi) - \rho W \\ \rho W \Pi \end{pmatrix}, \quad (9)$$

$$\mathbf{F}^i := \sqrt{\gamma} \begin{pmatrix} V^i D \\ \alpha S^i_j - \beta^i S_j \\ \alpha(S^i - v^i D) - \beta^i \tau \\ V^i D \Pi \end{pmatrix}, \quad (10)$$

$$\mathbf{S} := \sqrt{\gamma} \begin{pmatrix} 0 \\ \frac{1}{2} \alpha S^{ik} \partial_j \gamma_{ik} + S_i \partial_j \beta^i - (\tau + D) \partial_j \alpha \\ \alpha S^{ik} K_{ij} - S^j \partial_j \alpha \\ -(\alpha D / \tau_\Pi W) [\zeta (\vartheta + \Lambda - KW) + \Pi] \end{pmatrix}, \quad (11)$$

where we have introduced the following projections parallel and orthogonal to the unit vector $n^\mu := (1/\alpha, -\beta^i/\alpha)$:

$$D := -n_\mu J^\mu, \quad (12)$$

$$\tau := n_\mu n_\nu T^{\mu\nu} - D, \quad (13)$$

$$S_j := -\gamma_{j\mu} n_\nu T^{\mu\nu}, \quad (14)$$

$$S^i_j := \gamma^i_\mu \gamma_{j\nu} T^{\mu\nu}. \quad (15)$$

Furthermore, it is useful to remind that the expansion scalar takes the following form in the 3+1 split

$$\Theta := \nabla_\mu u^\mu = \vartheta + \Lambda - KW, \quad (16)$$

with

$$\vartheta := D_i (W v^i) = \frac{\partial_i (\sqrt{\gamma} W v^i)}{\sqrt{\gamma}}, \quad (17)$$

$$\Lambda := \frac{1}{\alpha} (\partial_t - \mathcal{L}_\beta) W + W v_i \hat{a}^i, \quad (18)$$

$$K := \gamma_{ij} K^{ij}. \quad (19)$$

The quantities D_i , \mathcal{L}_β , \hat{a}^i and K^{ij} denote the covariant derivative w.r.t. the purely spatial metric γ_{ij} , the Lie derivative

w.r.t. the shift vector, the acceleration of the normal observer $\hat{a}^i := \gamma^{ij} \partial_j \ln(\alpha)$ as well as the so-called extrinsic curvature, respectively.

We close this section by introducing the definition of the relativistic inverse Reynolds number based on [75]

$$\mathcal{R}^{-1} := \frac{\Pi}{p + e}. \quad (20)$$

From Eq. (20) it becomes clear that the Reynolds number measures the relative importance of inertial forces compared to viscous or dissipative forces.

A. Implementation

The simulations reported below are obtained after solving Einstein's equations together with the system of viscous second-order general-relativistic hydrodynamics (GRHD) equations in Eqs. (9)-(11) via the high-order high-resolution shock-capturing code `FIL` [22, 76]. The `FIL` code employs fourth-order accurate finite-difference stencils in Cartesian coordinates for the evolution of the constraint damping formulation of the Z4 formulation of the Einstein equations [77, 78]. The equations of viscous GRHD are solved with a fourth-order high-resolution shock-capturing scheme [79], the so-called `ECHO` scheme, built upon the open-source code `IllinoisGRMHD` [80]. More specifically, all flux terms appearing in Eq. (8) are discretized following the `ECHO` scheme and the source terms appearing in the last component of \mathbf{S} in Eq. (11) are discretized using finite differencing. Spatial derivatives are discretized using fourth-order central finite differences while the temporal derivative is calculated through first-order backward differencing w.r.t. the previous *full* timestep.

The discretization of the time derivative can be illustrated by the following example: Let us assume we employ Heun's second-order method with two stages and the solution should be advanced from t to $t + \Delta t$. The solution at $t - \Delta t$ is also available. Then, the first stage employs the approximation

$$\partial_t W|_t \approx \frac{W(t) - W(t - \Delta t)}{\Delta t}, \quad (21)$$

while in the second stage we use

$$\partial_t W|_{t+C\Delta t} \approx \frac{W(t + C\Delta t) - W(t)}{C\Delta t}, \quad (22)$$

where $C = 1$ for Heun's method. For higher-order multi-stage methods only C needs to be adjusted for each stage separately.

B. Primitive inversion and limiting

Typical methods for solving the equations of relativistic hydrodynamics involve the conversion from the evolved conserved variables to the primitive variables which has to be carried out numerically by using root-finding algorithms. In this

work, we augment the implementation of the purely hydrodynamical algorithm from [81] already provided in `FIL` in order to include the bulk-viscous pressure Π . As will be shown, almost all desirable properties, i.e., existence and uniqueness of solutions, can be transferred to the viscous case if a suitable limiting is employed. In the following, we just briefly review the most notable steps of the primitive inversion algorithm presented in [81] and highlight the modifications which arise from the inclusion of bulk viscosity. We omit all details related to the handling of the density floor, the finite range of the EOS table as well as all rescalings that follow from the bounds on the conserved and primitive variables. All of these steps are not influenced by the inclusion of bulk viscosity except that an atmosphere value for Π needs to be specified which we choose to be $\Pi_{\text{atmo}} = 0$.

We start by introducing the specific enthalpy $h := (e + p)/\rho$, the specific internal energy ϵ , the norm of the Eulerian three-velocity $v := \sqrt{v_i v^i}$ and, as in [81], the following definitions

$$a' := \frac{p + \Pi}{\rho(1 + \epsilon)}, \quad h' := h + \frac{\Pi}{\rho}, \quad z := Wv, \quad (23)$$

$$q := \frac{\tau}{D}, \quad r := \frac{S^i S_i}{D}, \quad k := \frac{r}{1 + q}. \quad (24)$$

These definitions yield the following relations:

$$z = \frac{r}{h'}, \quad \rho = \frac{D}{W}, \quad W = \sqrt{1 + z^2}, \quad (25)$$

and most crucially

$$\epsilon = Wq - zr + W - 1, \quad (26)$$

$$h' = (1 + \epsilon)(1 + a') = (W - zk)(1 + q)(1 + a'). \quad (27)$$

These expressions are exactly the same as in [81], if a and h are replaced by a' and h' , respectively.

1. Limiting

We now impose the same requirements as formulated in [81] on the viscous fluid of our simulations, i.e., the matter should satisfy the dominant energy condition and the viscous sound speed has to be smaller than the speed of light

$$0 \leq a' \leq 1, \quad (28)$$

$$0 \leq c_s'^2 < 1. \quad (29)$$

The quantity $c_s'^2$ is the square of the sound speed including modifications from bulk viscosity [55, 72, 82]

$$c_s'^2 = \frac{\zeta}{\tau_\Pi} \frac{1}{\rho h'} + \left(\frac{\partial p}{\partial e} \right)_\rho + \frac{1}{h'} \left(\frac{\partial p}{\partial \rho} \right)_e. \quad (30)$$

Because the bulk-viscous pressure Π is treated as an independent quantity and hence evolved along with the other typical hydrodynamic variables, the fluid can easily evolve into states which violate the conditions (28) and (29). Hence, we formulate the following limiting strategy in order to avoid large out-of-equilibrium contributions in the fluid:

(i) If $\Pi < 0$ and $\Pi < \sigma p$ with $-1 \leq \sigma \leq 0$, set $\Pi = \sigma p$. Note that for this range of the free parameter σ the condition (28) is automatically fulfilled. We typically choose $\sigma = -0.9$ in order to avoid regions where the fluid is pressureless, i.e., $p + \Pi = 0$.

(ii) If $\Pi > 0$ and $a' > 1$, set $\Pi = e - p$.

(iii) If $c_s'^2 > c_{\text{max}}^2$, set

$$\tau_\Pi = \frac{\zeta}{\rho h'} \left[c_{\text{max}}^2 - \left(\frac{\partial p}{\partial e} \right)_\rho - \frac{1}{h'} \left(\frac{\partial p}{\partial \rho} \right)_e \right]^{-1}, \quad (31)$$

where c_{max} is a free parameter between $0 \leq c_{\text{max}}^2 < 1$ in order explicitly ensure causality.

2. Bounds for the conserved variables

Again following [81], we find the same lower bound on q if the specific internal energy ϵ is required to be positive

$$q = h'W - 1 - \frac{p + \Pi}{W\rho} \geq \epsilon \geq \epsilon_{\text{min}}, \quad (32)$$

where ϵ_{min} denotes the minimum specific internal energy of the EOS. Additionally, we can also confirm that the same relations and bounds for the total momentum density in terms of k remain almost unchanged, i.e.,

$$k(v, a') = v \frac{1 + a'}{1 + v^2 a'}, \quad \frac{\partial}{\partial a'} k(v, a') \geq 0, \quad (33)$$

$$0 \leq \frac{1}{2} k \leq v \leq k \leq \frac{2v}{1 + v^2} < 1, \quad (34)$$

because we assume that the dominant energy condition is fulfilled. Imposing an upper limit on the velocity v , which we denote as v_{max} , then automatically yields

$$k < k_{\text{max}} = \frac{2v_{\text{max}}}{1 + v_{\text{max}}^2}. \quad (35)$$

3. Root finding, existence and uniqueness

We use the same root finding function as in [81] except that we substitute $h(z)$ by $h'(z)$, i.e.,

$$f(z) = z - \frac{r}{h'(z)}. \quad (36)$$

Note that we omit the \sim superscript compared to [81] for simplicity. Furthermore, the limits are imposed at every step of the root finding which means that when computing $a'(z)$ we impose the requirements (i) and (ii). Then, the limited value for $a'(z)$ is used in Eq. (27) to calculate $h'(z)$.

From Eq. (34) we find that the bracketing interval remains unchanged as well

$$z_- = \frac{k/2}{\sqrt{1 - k^2/4}}, \quad z_+ = \frac{k}{\sqrt{1 - k^2}}. \quad (37)$$

It is possible to show that $f(z)$ has one unique solution by following the steps outlined in [81] and replacing h and a by h' and a' , respectively. There is only one notable difference: Due to the fact that we limit Π in the root finding process, it can only be considered constant if the limiter is never applied. This leads to three cases for which uniqueness can be established separately. Overall, we obtain three different relations for the quantity B defined through

$$\frac{df}{dz} = 1 - v^2 B, \quad (38)$$

$$B = a' \left[1 + \frac{\partial \ln(1 + a')}{\partial \ln(1 + \epsilon)} \right] + \frac{\partial \ln(1 + a')}{\partial \ln(\rho)}. \quad (39)$$

If Π is assumed to be constant, then we obtain

$$B_{\Pi} = \frac{\partial p}{\partial e} \Big|_{\rho} + \frac{1}{h'} \frac{\partial p}{\partial \rho} \Big|_e \leq c_s'^2 < 1. \quad (40)$$

If Π is limited from below, then we obtain

$$B_{(i)} = (1 - \sigma) \left\{ \frac{\partial p}{\partial e} \Big|_{\rho} + \frac{\rho}{(1 - \sigma)p + e} \frac{\partial p}{\partial \rho} \Big|_e \right\} \leq c_s'^2 < 1. \quad (41)$$

Finally, if Π is limited from above, then we obtain

$$B_{(ii)} = a' = 1. \quad (42)$$

4. Reynolds number limits

In this section we want to give an estimate for the minimum and maximum inverse Reynolds numbers, \mathcal{R}_{\min}^{-1} and \mathcal{R}_{\max}^{-1} , respectively, e.g., see Eq. (20), achievable by our scheme. For that we employ the simple ideal fluid EOS, i.e., $p = (\Gamma_{\text{id}} - 1)\rho\epsilon$, where Γ_{id} denotes the adiabatic index. For an isentropic fluid which obeys the ideal fluid EOS we can express the pressure additionally as $p = \kappa\rho^{\Gamma_{\text{id}}}$ such that the specific internal energy can be written as $\epsilon = \kappa\rho^{\Gamma_{\text{id}}-1}/(\Gamma_{\text{id}} - 1)$. The minimum inverse Reynolds number is given by (i):

$$\mathcal{R}_{\min}^{-1} = \frac{\sigma p}{e + p} = \sigma \frac{1}{\kappa^{-1}\rho^{1-\Gamma_{\text{id}}} + 1 + (\Gamma_{\text{id}} - 1)^{-1}}. \quad (43)$$

A typical choice for test simulations of neutron stars is $\Gamma_{\text{id}} = 2$, $\kappa = 100$ and $\rho = 0.00128$ which yields $\mathcal{R}_{\min}^{-1} \simeq -0.1$ for $\sigma = -0.9$. The maximum inverse Reynolds number is given by (ii):

$$\mathcal{R}_{\max}^{-1} = \frac{e - p}{e + p} = \frac{(\Gamma_{\text{id}} - 1)\rho^{1-\Gamma_{\text{id}}}/\kappa - \Gamma_{\text{id}} + 2}{(\Gamma_{\text{id}} - 1)\rho^{1-\Gamma_{\text{id}}}/\kappa + \Gamma_{\text{id}}}. \quad (44)$$

Using the same choice for Γ_{id} , κ and ρ we find $\mathcal{R}_{\max}^{-1} \simeq 0.8$.

C. Transport coefficients and transition to inviscid fluid

As already mentioned, the scope of this work is to examine, for the first time, the impact of a causal and constant

bulk viscosity prescription on BNS merger simulations. However, as neutron star mergers lead to violent shocks propagating outward through a decreasing density profile, a constant value for the bulk viscosity which is applicable in the high-density regime will lead to large inverse Reynolds numbers as soon as the shock reaches sufficiently low densities. As a consequence, our limiting procedure will have to be applied continuously in the low density regime. Thus, we implement a smooth transition zone between the high-density bulk viscosity ζ_h and the low density bulk viscosity ζ_l typically chosen to be $\zeta_l = 0$. The high-density zone which has $\zeta = \zeta_h$ occupies matter with densities $\rho \geq \rho_h$ while the region with densities $\rho \leq \rho_l$ has $\zeta = \zeta_l$. The functional behaviour of the bulk viscosity in the transition zone defined as the density interval $\rho_l < \rho < \rho_h$ is expressed through a cubic polynomial which ensures continuity of ζ and $d\zeta/d\rho$ at ρ_h and ρ_l . We have found that using a cubic polynomial in place of a simple linear interpolation leads to bulk viscosity with better functional behaviours.

Overall, our prescription can be summarized as follows:

$$\zeta(\rho) = \begin{cases} \zeta_l & \text{if } \rho \leq \rho_l, \\ a\rho^3 + b\rho^2 + c\rho + d & \text{if } \rho_l < \rho < \rho_h, \\ \zeta_h & \text{if } \rho \geq \rho_h, \end{cases} \quad (45)$$

where the coefficients of the cubic polynomial are given by

$$a = 2(\zeta_l - \zeta_h)/(\rho_h - \rho_l)^3, \quad (46)$$

$$b = 3(\rho_l + \rho_h)(\zeta_h - \zeta_l)/(\rho_h - \rho_l)^3, \quad (47)$$

$$c = 6\rho_h\rho_l(\zeta_l - \zeta_h)/(\rho_h - \rho_l)^3, \quad (48)$$

$$d = [(3\rho_h\rho_l^2 - \rho_l^3)\zeta_h + (\rho_h^3 - 3\rho_h^2\rho_l)\zeta_l]/(\rho_h - \rho_l)^3. \quad (49)$$

Additionally, the relaxation time is set to be constant using a prescription with a linear interpolation in the transition zone

$$\tau_{\Pi}(\rho) = \begin{cases} \tau_l & \text{if } \rho \leq \rho_l, \\ \tau_h - m(\rho_h - \rho) & \text{if } \rho_l < \rho < \rho_h, \\ \tau_h & \text{if } \rho \geq \rho_h, \end{cases} \quad (50)$$

where

$$m = (\tau_h - \tau_l)/(\rho_h - \rho_l). \quad (51)$$

In contrast to the bulk viscosity ζ , we found that a linear functional form for τ in the transition zone is sufficient to ensure numerical stability. We typically choose τ_h to be $\sim 1.1\Delta t_{\min}$ and τ_l to be $\sim 1.1\Delta t_{\max}$, where Δt_{\min} and Δt_{\max} are the minimum and maximum timesteps in the simulation, respectively. If the neutron stars are fully covered by the highest refinement level and the hydrodynamical timescale is well-resolved by Δt_{\min} , this prescription for the relaxation time ensures that $\Pi \simeq \Pi_{\text{NS}} = -\zeta\Theta$ and the avoidance of stiff sources. Note that at the same time causality is guaranteed through Eq. (31) which can lead to a local increase of τ_{Π} .

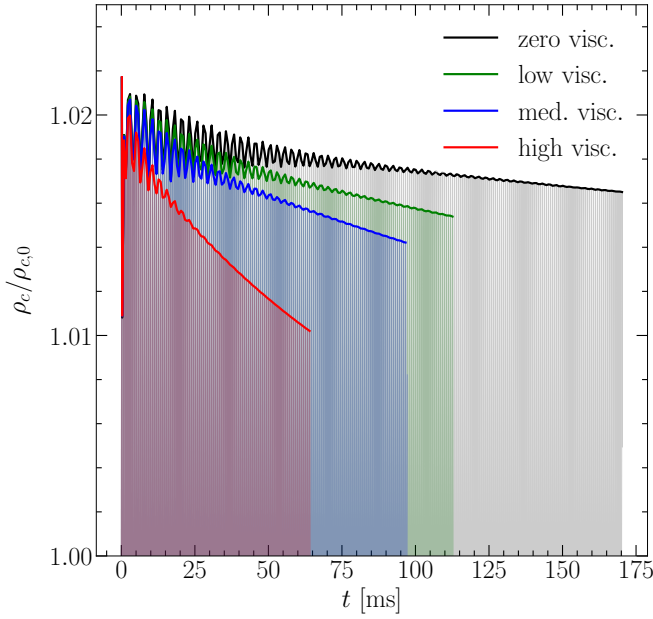


FIG. 1. Shown in solid transparent lines is the timeseries of the central rest-mass density normalized by its value at $t = 0$ for the zero (black line), low (green line), medium (blue line) and high (red line) viscosity case. We present only results from the highest resolution simulations, i.e., $\Delta x \approx 207$ m. Solid thick lines of the corresponding color show the envelope of $\rho_c/\rho_{c,0}$ which illustrates the impact of different bulk viscosities on the damping time of linear density oscillations.

III. RESULTS

A. Oscillating neutron stars and numerical viscosity

We now move on to the first numerical experiments involving isolated neutron stars in order to test the implementation. Specifically, we investigate the damping of radial perturbations of a neutron star in full general relativity. In this test, we set out to measure the numerical and physical viscosity of our code. The procedure has been laid out in [83] and we follow it for the most part except of some minor differences. A detailed account of the measurement procedure employed in this work is presented in Appendix A. In short, we extract the damping time of central density oscillations from our simulations and use it to obtain an estimate for ζ_h .

We use simulations of isolated TOV stars using a simple hybrid polytropic EOS [52], i.e.,

$$p = \kappa \rho^\Gamma + (\Gamma_{\text{th}} - 1) \rho \epsilon_{\text{th}}, \quad (52)$$

with $\kappa = 100$, $\Gamma = 2$, $\Gamma_{\text{th}} = 1.1$ and a central density of $\rho_c = 1.28 \times 10^{-3} M_\odot^{-2} \approx 7.91 \times 10^{14} \text{ g cm}^{-3}$. The quantity ϵ_{th} denotes the thermal component of the specific internal energy. This setup yields a $M = 1.4 M_\odot$ star, where M denotes the Arnowitt-Deser-Misner (ADM) mass, with a radius of $R = 14.2$ km. This configuration is well-explored with known pulsation frequencies [84]. We use such a low Γ_{th} because we have found that the drift of ρ_c can be reduced, if Γ_{th}

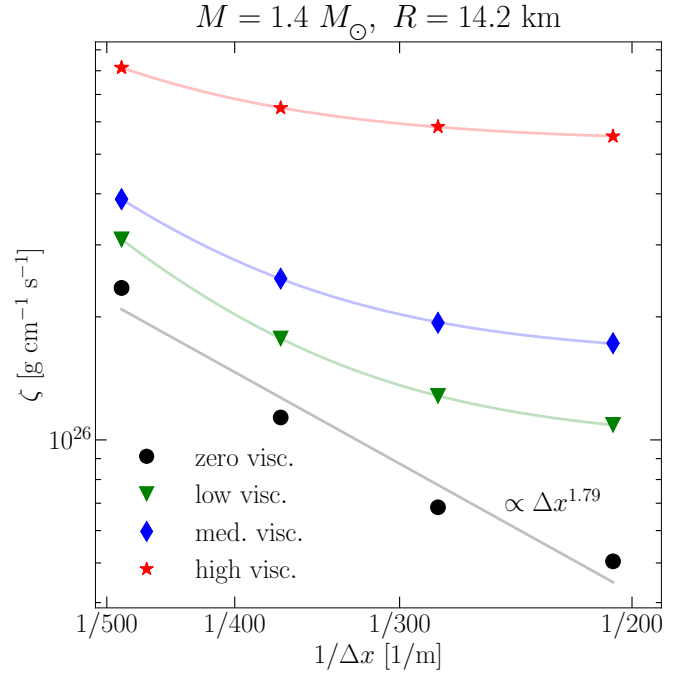


FIG. 2. Different symbols denote measured values of the bulk viscosity calculated by employing the damping time of central density oscillations of perturbed TOV solutions. We present the zero, low, medium and high-viscosity case using black circles, green triangles, blue diamonds and red stars, respectively. Transparent solid lines of the corresponding color display fits to the measured values as a function of grid resolution. The transparent black line shows a linear fit of $\log[\zeta]$ as a function of $\log[\Delta x]$ for the zero-viscosity case. The parameters of the TOV solution are given in the title.

assumes values close to but larger than 1.

Overall, we carry out 16 simulations which correspond to four different bulk viscosities and four different resolutions. We vary the bulk viscosity between $\zeta_h \in [0, \sim 9.42 \times 10^{25}, \sim 1.98 \times 10^{26}, \sim 8.20 \times 10^{26}] \text{ g s}^{-1} \text{ cm}^{-1}$, which are denoted as zero, low, medium and high-viscosity cases, respectively. The resolution on the finest refinement level varies between $\Delta x \in \{\sim 207, \sim 281, \sim 369, \sim 487\} \text{ m}$. Furthermore, we set $\zeta_l = 0$, $\rho_h = 1.28 \times 10^{-4} M_\odot^{-2} \approx 7.91 \times 10^{13} \text{ g cm}^{-3}$ and $\rho_l = 1.28 \times 10^{-7} M_\odot^{-2} \approx 7.91 \times 10^{10} \text{ g cm}^{-3}$.

We initialize the stars by using a perturbation in the form of the fundamental radial eigenmode. The perturbation produces oscillations in the central density on the order of $\sim 2\%$, e.g., see Fig. 1 which shows damped density oscillations of ρ_c normalized by its initial value at $t = 0$, i.e., $\rho_c/\rho_{c,0}$ with $\rho_{c,0} := \rho_c(t = 0)$. We present the zero, low, medium and high-viscosity case using a black, green, blue and red line, respectively. All cases shown in Fig. 1 are simulated at the highest resolution, i.e., $\Delta x \approx 207$ m. Such a small oscillation amplitude ensures that our simulations remain in the linear regime of the coupled viscous hydrodynamic and gravitational equations. The perturbation is initialized by using the `PizzaTOV` thorn which is part of the publicly available thorns accompanying the `WhiskyTHC` code [85, 86] built

Model	ζ_a	ζ_s	p_h
	$[\text{g s}^{-1} \text{cm}^{-1}]$	$[\text{g s}^{-1} \text{cm}^{-1}]$	
zero visc.	—	4.4×10^{29}	1.79
low visc.	9.89×10^{25}	8.87×10^{32}	3.57
med. visc.	1.6×10^{26}	5.65×10^{32}	3.45
high visc.	5.36×10^{26}	2.75×10^{32}	3.23

TABLE I. Fitting results to the measured bulk-viscosity values presented in Fig. 2 using Eq. (53) with $\lambda \approx 3.48 \times 10^4 \text{ m}$.

upon the `Einstein Toolkit` [87].

During the simulations the perturbed stars oscillate almost entirely in their fundamental radial eigenmode whose amplitude decays over time. However, especially for the zero-viscosity case, the oscillations are weakly contaminated by higher-order modes at early times, as can be seen in Fig. 1. The damping time of the amplitude is related to the magnitude of ζ_h such that larger bulk viscosities lead to shorter damping times.

The amplitude of the oscillations is subject to two damping mechanisms, namely numerical and physical damping. The numerical damping stems from a finite grid resolution and gives rise to a so-called numerical viscosity which vanishes in the limit of infinite grid resolution. The physical damping is related to our implementation of bulk viscosity and is independent of grid resolution. Figure 2 shows the values of ζ obtained through our measurement procedure for all 16 simulations denoted by different symbols. Additionally, we present fits to the measured viscosities as a function of grid resolution in transparent lines. For nonzero input viscosities, i.e., nonzero ζ_h , we use the formula

$$\zeta(\Delta x) = \zeta_a + \zeta_s(\Delta x/\lambda)^{p_h}, \quad (53)$$

where ζ_a is the asymptotically measured viscosity at infinite grid resolution, ζ_s is a numerical viscosity scale, p_h is the convergence order and $\lambda = 2\pi c_s \omega^{-1}$ is the wavelength of the perturbation with ω being its angular frequency. For the zero viscosity case we employ a linear fit of $\log[\zeta]$ as a function of $\log[\Delta x]$ which is equivalent to setting $\zeta_a = 0$ in Eq. (53). We make this choice because keeping ζ_a as an independent fitting coefficient in the zero-viscosity case, which could possibly assume values not equal to zero, would lead to overfitting of the data and misleading results for p_h . The results for all fitting coefficients are shown in Table I.

There is a number of observations that can be made. First, all nonzero-viscosity cases lead to measured bulk viscosities that decrease as the resolution is increased (the cell size is smaller) and that asymptote to a constant value. This confirms that, for high enough resolutions, the damping of the corresponding density oscillations is independent of the employed cell size.

Bearing in mind that the measured viscosity ζ_a and the input viscosity ζ_h are distinct but mathematically and physically related, when comparing the values of ζ_a with those of ζ_h we find a good agreement notwithstanding the approximations involved in deriving the formulas for the measurement of ζ_a ,

see e.g., Appendix A. More specifically, we find an agreement of $\lesssim 6\%$, $\lesssim 20\%$ and $\lesssim 35\%$ for the low, medium and high-viscosity case, respectively. The reasons for the observed differences can be numerous, e.g., the usage of Newtonian formulas, a varying numerical and physical viscosity profile within the star, or the influence of discretization errors from the neutron star surface. An additional, and possibly strong, assumption is that the Newtonian damping time calculated through the relation between oscillatory kinetic energy and the corresponding energy dissipation in Eq. (A2) of Appendix A continues to give a good approximation for the damping time of the density oscillations in fully general-relativistic evolutions of TOV stars. In summary, given the perturbative nature of our study, we have found that Eq. (A2) approximates reasonably well the damping of ρ_c .

Second, we observe slow convergence of the numerical viscosity in the zero-viscosity case. The `FIL` code employs 4th-order accurate methods for the discretization in space, see [76], while the employed time integrator is of order three. This means that the observed convergence order of ~ 1.79 is far below the formal one. Note that the discretization of Θ in Eq. (6) does not impact the convergence order for the zero-viscosity case. We suspect that this behaviour is related to the influence of discretization errors from the neutron star surface whose ill-balanced density and pressure gradients manifest as effective discontinuities in the numerical solution. This leads to a reduction of the observed convergence order. However, it is interesting to note that we were able to recover the correct formal convergence order in similar simulations employing smaller neutron stars, i.e., TOV solutions with a smaller radius. We report on these findings in Appendix B.

B. Migration of neutron stars and propagation of shock waves

In this test, we simulate a migrating TOV star [84] with four different values for the bulk viscosity, i.e., $\zeta \in [0, 4 \times 10^{28}, 2 \times 10^{29}, 10^{30}] \text{ g s}^{-1} \text{cm}^{-1}$, which are denoted as zero, low, medium and high viscosity cases, respectively. We use the same hybrid polytropic EOS as in the numerical viscosity measurement, see Eq. (52), and choose $\kappa = 100$ and $\Gamma = \Gamma_{\text{th}} = 2$. As in [84] the stars are initialized to have a central rest-mass density of $\rho_c = 8 \times 10^{-3} M_\odot^{-2} \approx 4.94 \times 10^{15} \text{ g cm}^{-3}$ which results in a mass of $M = 1.447 M_\odot$. Furthermore, the computational grid has outer boundaries at $64 M_\odot \simeq 95 \text{ km}$ in the three spatial directions and we employ a z -symmetry in the equatorial plane. We use four refinement levels with a factor of two refinement; the last level, which has a width of $24 M_\odot \simeq 35 \text{ km}$ has a grid spacing of $\Delta x = 0.25 M_\odot \simeq 370 \text{ m}$.

We start by describing the evolution of the characteristic central quantities shown in Fig. 3. The left panel shows the evolution of the central rest-mass density normalized by its initial value at $t = 0$ for all four cases in different colors. First, as expected, the magnitude of ζ has a strong influence on the damping time of the nonlinear central density oscillations. As already observed in the numerical viscosity measurement, higher values for the bulk viscosity lead to smaller values for

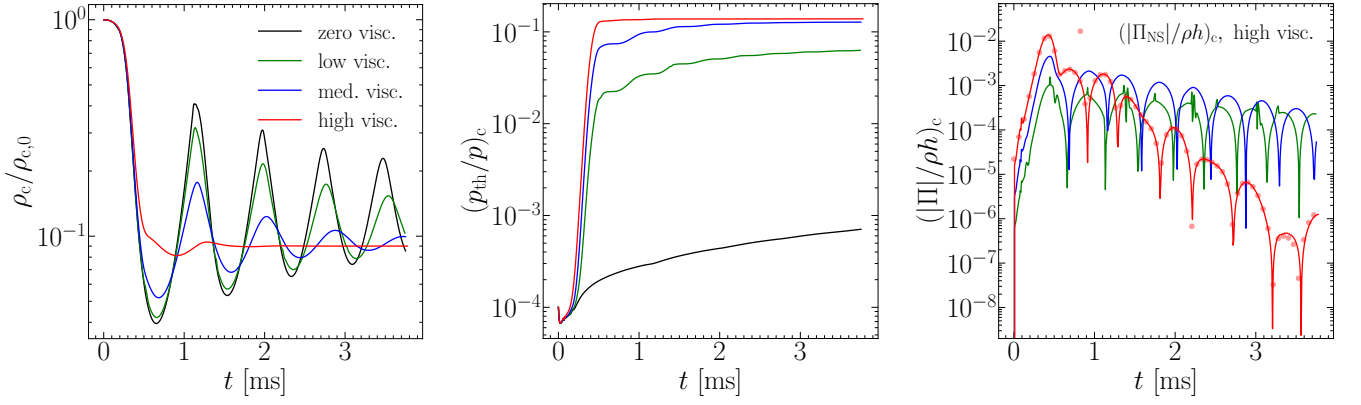


FIG. 3. Shown are the normalized density (left panel), the ratio of the thermal pressure over the total pressure (middle panel) and the absolute inverse Reynolds number (right panel), i.e., the ratio of the absolute value of the bulk-viscous pressure over the enthalpy density, in the center of the migrating neutron star for the zero (black lines), low (green lines), medium (blue lines) and high (red lines) viscosity case. The transparent red symbols in the right panel denote the ratio of the absolute NS value over the enthalpy density for the high-viscosity case.

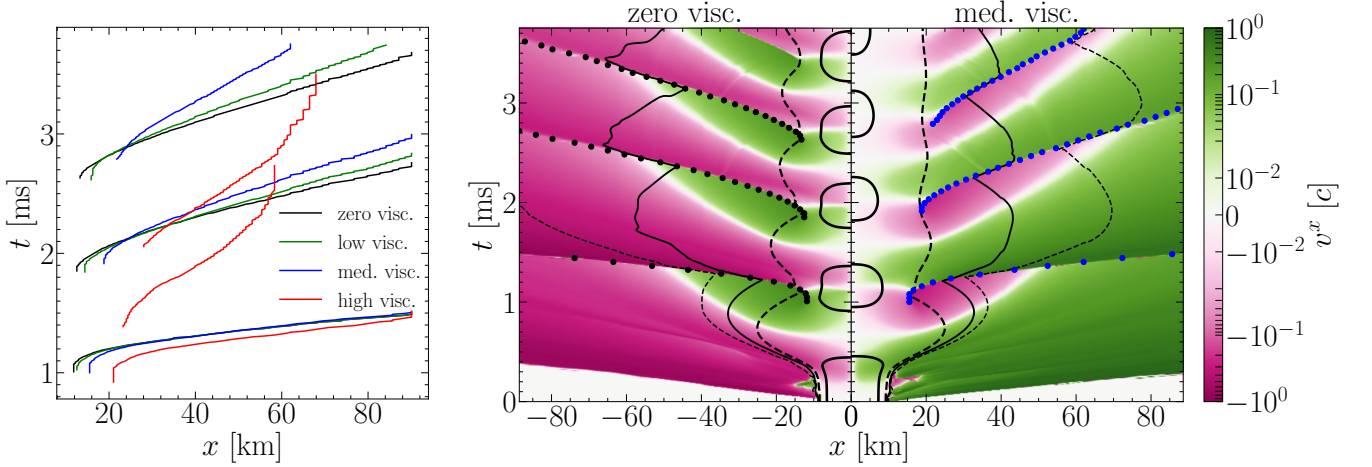


FIG. 4. *Left*: Spacetime diagram of the evolution of the shock fronts on the x -axis which develop at the neutron star surface as a result of the violent nonlinear oscillations during the migration of the neutron star. We present the zero, low, medium and high viscosity case using black, green, blue and red lines, respectively. *Right*: Spacetime diagrams of the evolution of the x -component of the Eulerian three-velocity on the x -axis for the zero (left half) and medium-viscosity (right half) case. The symbols denote the evolution of the corresponding shock fronts already presented in the *left* panel. The inner solid, inner dashed, outer solid and outer dashed lines denote density contours at $\rho = 4.5 \times [10^{14}, 10^{12}, 10^{10}, 10^8] \text{ g cm}^{-3}$, respectively. Note that the inner solid line represents ρ_h while the outer solid line corresponds to ρ_t , see also Eq. (45).

the damping time such that the nonlinear oscillations of ρ_c decay more efficiently.

Additionally, we observe that the average value around which these oscillations occur decreases with increasing bulk viscosity. This can be understood by looking at the middle panel in Fig. 3 which shows the evolution of the central thermal pressure component $p_{th} := (\Gamma_{th} - 1)\rho\epsilon_{th}$ normalized by the central total pressure p . Higher values for ζ lead to a more rapid initial increase and higher asymptotic values of p_{th}/p in the center of the star. As a result, the migrating TOVs with a larger value for the bulk viscosity have larger thermal support which leads to less compact asymptotic states with a smaller central rest-mass density.

Finally, the right panel of Fig. 3 shows the absolute value

of the relativistic inverse Reynolds number in the center of the stars. The quantity \mathcal{R}^{-1} can be used to gain intuition into estimating the importance of viscous effects in a generic relativistic hydrodynamic flow while also quantifying the applicability of the system of equations employed to describe out-of-equilibrium effects. Regarding the former, we observe a dramatic influence of viscous effects on the evolution of the central-rest mass density for a flow with $|\mathcal{R}^{-1}| \gtrsim 10^{-2}$. Regarding the latter, we conclude that our simulations are still in a regime where the equations employed remain in their domain of applicability due to the low inverse Reynolds number. Additionally, the red transparent circles show the inverse Reynolds number computed from the NS value for the high-viscosity case. We observe good agreement between the true

bulk-viscous pressure Π and Π_{NS} which means that our simulations deviate only very weakly from a first-order formulation of relativistic dissipative hydrodynamics while at the same time being fully causal. Note that NS values are presented only for the high-viscosity case to avoid overcrowding the figure. However, we observe the same agreement for the low and medium-viscosity case.

Now, we move on to the evolution of shock waves commonly observed in migration tests. Our results are visualized in Fig. 4. The left panel of Fig. 4 shows a spacetime diagram of the evolution of the first three shock fronts appearing for each value of the bulk viscosity ζ on the x-axis of our simulations. The right panel shows spacetime diagrams of the Eulerian three-velocity on the x-axis, i.e., $v^x(x, y = 0, z = 0)$, for the zero (left half) and medium viscosity (right half) case. Additionally, we use black contour lines to plot the evolution of the density contours at $\rho \in [4.5 \times 10^{14}, 10^{12}, 10^{10}, 10^8] \text{ g cm}^{-3}$ using solid, dashed, solid and again dashed line styles, respectively. Note that the inner solid line represents ρ_h while the outer solid line corresponds to ρ_l , see Eq. (45). The colored markers denote the locations of the first three shock fronts for each of the two simulations, respectively.

First, we observe that a larger value for the bulk viscosity leads to a shock front which develops at larger distances from the core. In order to understand this, we need to describe briefly the generic mechanism of shock-front formation. Prior to the development of the shock front, the neutron star is contracting and matter at larger distances is radially infalling. As soon as the contraction of the neutron star is decelerated as the result of increasing pressure gradients, radially infalling material hits the neutron star surface and gets shocked. Consequently, an outward propagating shock is generated as soon as the shock is strong enough to overcome the ram pressure generated by the radially infalling material.

We find in the right panel of Fig. 4 that the inner solid density contour line of the zero-viscosity case reaches larger values in x than the corresponding density contour line in the medium-viscosity case. This indicates that the neutron star in the medium-viscosity case has a less compact core which can be explained by the additional thermal support observed in Fig. 3. At the same time a larger density gradient is present in the outer layers of the medium-viscosity case which can be seen by comparing distances between neighbouring density contour lines. As a result, the pressure gradient in the outer layers of the medium-viscosity star is increased which means that the neutron star surface and the location where the shock forms have moved outwards in comparison to the zero-viscosity case.

Second, we observe that larger values for the bulk viscosity lead to less energetic shock waves, especially when considering the second and third shock wave. This can be seen in the left panel of Fig. 4 when concentrating on the second shock wave for each value of the bulk viscosity. Clearly, the velocities of the shock fronts decrease with higher ζ . In the high-viscosity case the shock front of the second wave even stops propagating when it reaches $\sim 60 \text{ km}$. The reason for this behaviour is mainly related to the damping of the neutron

star oscillations due to viscosity. For the viscous cases matter is still radially infalling and being shocked at the neutron star surface. But due to the increased dissipative transfer of radial kinetic energy to thermal energy in the neutron star a lower energy budget is available to accelerate the shock. Hence, the shocks become weaker.

C. Binary neutron star mergers

1. Simulation setup

In this section we discuss the simulations of BNS mergers with a constant and causal bulk-viscosity prescription. We use the initial data setup presented in [47] which produces a long-lived HMNS remnant. Similar to the numerical experiments with isolated stars, we employ a hybrid EOS of the form $p = p_{\text{cold}} + \rho \epsilon_{\text{th}} (\Gamma_{\text{th}} - 1)$ where the cold part is modeled by a cold, β -equilibrated slice of the `TNTYST` EOS [88]. We choose $\Gamma_{\text{th}} = 1.7$ which corresponds to the optimal value found in [89]. We simulate four different values for the bulk viscosity ζ which is given by $\zeta_h \in [\zeta_0, \zeta_0/2, \zeta_0/5, 0]$ with $\zeta_0 = 10^{30} \text{ g cm}^{-1} \text{ s}^{-1}$. The value of ζ_0 corresponds approximately to the highest bulk viscosity observed in the [44]. In accordance with the magnitude of ζ the simulations are labeled as high, medium, low and zero viscosity case. We choose $\rho_h \approx 4.52 \times 10^{14} \text{ g cm}^{-3}$ and $\rho_l \approx 1.13 \times 10^{12} \text{ g cm}^{-3}$. Besides, we have set $\tau_h \approx 2.7 \times 10^{-4} \text{ ms}$.

All reported simulations are performed with a resolution of $\Delta x \sim 0.17 M_\odot \approx 260 \text{ m}$ on the sixth refinement level. We have also performed simulations with a lower resolution of $\Delta x \sim 0.25 M_\odot \approx 370 \text{ m}$ for the zero, low and high viscosity case. We observe qualitatively consistent behaviour such that we only report the results of the high-resolution simulations.

2. Thermal properties

In this subsection we discuss the impact of bulk viscosity on thermal properties of BNS mergers. We start by reporting the maximum rest-mass density in the left panel of Fig. 5 and the thermal energy

$$E_{\text{th}} := \int \rho \epsilon W \sqrt{\gamma} dx dy dz, \quad (54)$$

in the middle panel of Fig. 5. The integral in Eq. (54) is calculated over the whole simulation domain.

First, from the inset in the left panel of Fig. 5 we observe that the strong density oscillations which occur during the first $\sim 5 \text{ ms}$ after merger are damped efficiently in the cases with strong bulk viscosities. This is not surprising as these oscillations are related to expansion and compression cycles of the newly formed HMNS. It is precisely the kinetic energy stored in fluid expansion and compression which is dissipated through bulk viscosity. Furthermore, we observe that a larger bulk viscosity leads to a less dense HMNS core at the end of our simulations at around $t - t_{\text{mer}} \approx 24 \text{ ms}$. This effect is related to the increase in the kinetic rotational energy

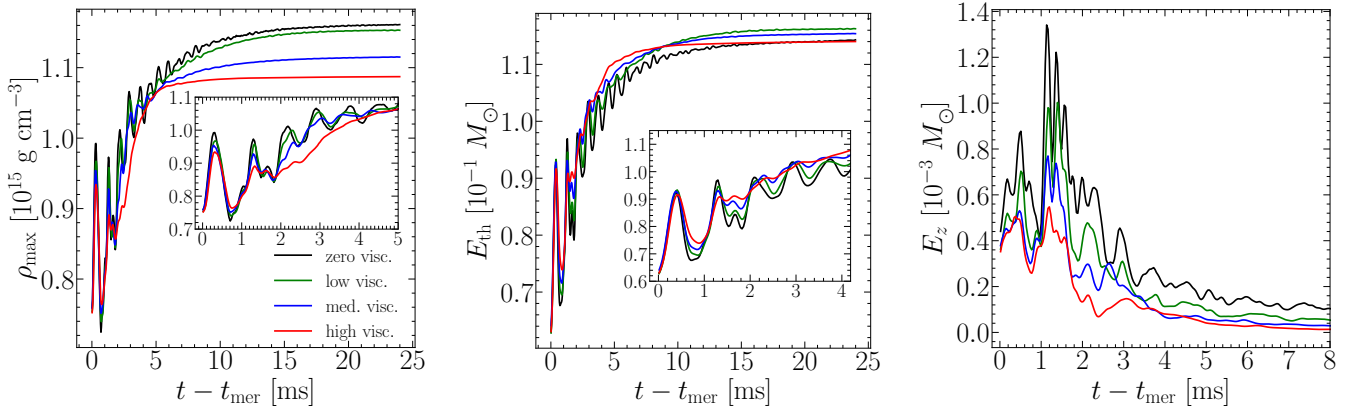


FIG. 5. *Left*: Maximum rest-mass density in the postmerger phase for the zero (black line), low (green line), medium (blue line) and high (red line) viscosity case. The inset shows a zoom-in for the first five milliseconds. *Middle*: Same as *left* panel but for the total thermal energy defined in Eq. (54). *Right*: Same as *left* panel but for the total z -directed kinetic energy defined in Eq. (55).

which adds centrifugal support to matter located in the densest regions of the HMNS (see Appendix C for details). Note that in contrast to the constant bulk-viscosity prescription applied in this work, a microphysical model leads to a denser and more compact remnant with constant kinetic rotational energy across different magnitudes of ζ [47].

Second, from the middle panel of Fig. 5 we find that larger bulk viscosities lead to a larger overall thermal energy in the first ~ 5 ms after merger. As observed before, during the first ~ 5 ms after merger the damping of large density oscillations is most efficient such that also the dissipation of kinetic into thermal energy is most efficient. Thus, larger bulk viscosities lead to larger thermal energies during that time. However, after the first five milliseconds other effects need to be taken into account in order to explain the evolution of E_{th} . While the dissipation of kinetic into thermal energy leads to an increase in thermal energy the aforementioned decrease in central rest-mass density leads to a decrease in thermal energy as the HMNS core is less dense as a result of the additional centrifugal support. Both of these effects are competing on a timescale larger than five milliseconds which leads to the non-monotonic behaviour observed in E_{th} at the end of our simulations. In particular, we see that the decrease in central density of the medium and high-viscosity cases leads to *lower* final thermal energies than in the low viscosity case which has the largest final thermal energy. The final thermal energy of the high-viscosity case is even below the inviscid case.

Finally, we show the z -directed kinetic energy in the simulation domain

$$E_z := \frac{1}{2} \int \rho h v^z u_z \sqrt{\gamma} dx dy dz, \quad (55)$$

in the right panel of Fig. 5. In order to strengthen the claim that during the first ~ 5 ms after the merger most of the bulk-viscous energy dissipation is taking place we can make use of E_z . This is illustrative as the kinetic energy in the z -direction is generated purely by strong oscillations and shocks coming from the collision of the binary and is therefore subject to bulk-viscous damping. Here, we see very clearly that the

behaviour is monotonic and larger bulk viscosities lead to a smaller E_z . Additionally, we also verify that most of the kinetic energy is dissipated during the first ~ 5 ms after merger.

Furthermore, we can also evaluate “how viscous” the fluid is or in other words, how large the deviations from thermodynamic equilibrium are by measuring the relativistic Reynolds number \mathcal{R} defined in Eq. (20). We present the quantity $|\mathcal{R}^{-1}|$ measured in the center of the grid for the first ~ 5 ms after merger in the left panel of Fig. 6 and $|\Pi|/p$ measured in the center of the grid for the same time interval in the right panel. We present timeseries for all simulations and additionally show the quantities $(|\Pi|_{\text{NS}}/\rho h)_c$ and $(|\Pi|_{\text{NS}}/p)_c$ denoted by red transparent lines and circles in both panels for the high-viscosity case, see also Eq. (7).

Both panels show qualitatively the same behaviour: Larger bulk viscosities lead to a larger inverse Reynolds number as well as larger viscous contributions to the total pressure. It is interesting to note that for the high-viscosity case the inverse Reynolds number reaches values above $\sim 1\%$ which corresponds to a bulk-viscous pressure that is $\sim 20\%$ of the equilibrium pressure. This happens right after merger when the strongest density oscillations are present. Afterwards, both quantities decrease but remain of this order until $t - t_{\text{mer}} \approx 1.5$ ms.

Then, both quantities drop sharply by approximately two orders of magnitude and, after further decrease, reach values of around $(|\Pi|/\rho h)_c \approx 10^{-5}$ and $(|\Pi|/p)_c \approx 10^{-4}$ at $t - t_{\text{mer}} \approx 5$ ms. This provides further evidence that bulk-viscous dissipation works very efficiently only in the first five milliseconds after merger; Figure 6 even suggests that during the first 1.5 ms after merger bulk-viscous dissipation is having the biggest impact on the merger. Additionally, similar to the results presented for the migration test in Fig. 3, we observe good agreement between the true bulk-viscous pressure Π and Π_{NS} for all viscosity cases (note that NS values are presented only for the high-viscosity case to avoid overcrowding the figure).

The measurement of the relativistic Reynolds number enables us to compare out-of-equilibrium contributions in BNS

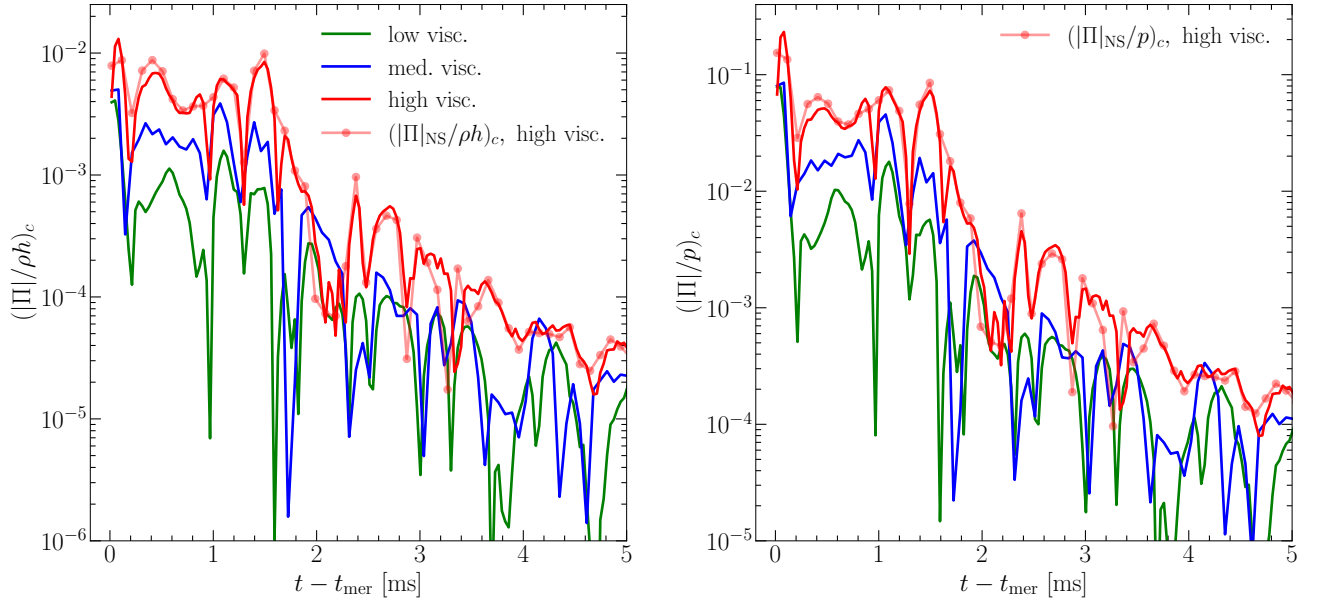


FIG. 6. *Left*: Absolute inverse Reynolds number, i.e., the ratio of the absolute bulk-viscous pressure over the enthalpy density, for the zero (black line), low (green line), medium (blue line) and high (red line) viscosity case. Transparent red circles denote the same quantity but calculated from the NS value for the high-viscosity case. *Right*: Same as *left* panel but for the ratio of the absolute bulk-viscous pressure over the EOS pressure.

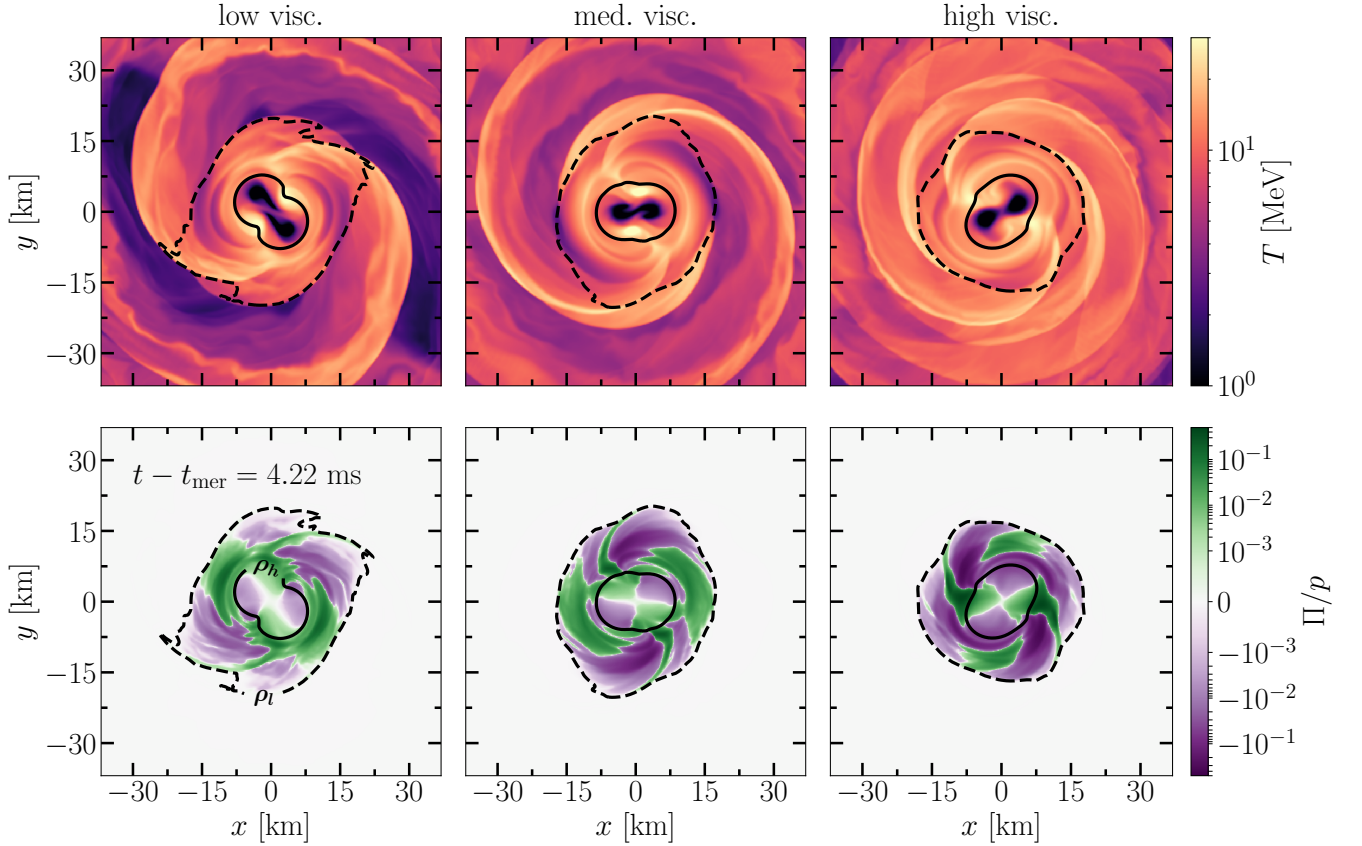


FIG. 7. Cross-sections of the temperature (top row) and of the ratio of the bulk-viscous pressure over the EOS pressure (bottom row) in the (x, y) plane at $z = 0$. The snapshots are taken at $t - t_{\text{mer}} = 4.22$ ms. Shown are the low viscosity (left column), medium viscosity (middle column) and high-viscosity (right column) cases. The solid line denotes a density contour at $\rho = \rho_h$ while the dashed line denotes a density contour at $\rho = \rho_l$.

mergers to the viscous contributions in other relativistic fluids, namely the quark-gluon plasma (QGP) encountered in heavy-ion collisions (HICs). Following the results presented in [37], we first observe that the order-of-magnitude estimates obtained in that study through post-process calculations agree with our findings for the highest viscosity case. This is not surprising as [37] presents the maximum inverse Reynolds number over the whole domain which is likely found where the bulk viscosity ζ reaches its maximum. Since our high-viscosity case makes use of a constant value for ζ which corresponds to the highest value found in [37], it is natural to expect similar inverse Reynolds numbers if the underlying fluid motion does not vary significantly.

Second, as observed in [37] we find that the inverse Reynolds number in HICs is approximately one order of magnitude higher than in BNS mergers suggesting that the QGP is further away from thermodynamic equilibrium than the high-density matter encountered in a HMNS shortly after merger.

Next, we report in Fig. 7 sections of the temperature distribution (top row) and the distribution of the quantity Π/p (bottom row) in the equatorial plane at $t - t_{\text{mer}} \approx 4.22$ ms for the low (left column), medium (middle column) and high viscosity (right column) cases. The solid line denotes a density contour at $\rho = \rho_h$ while the dashed line denotes a density contour at $\rho = \rho_l$. During this time the strong damping of density oscillations and thus the dissipation of oscillatory kinetic energy into thermal energy has almost ended, as discussed previously. However, the HMNS has not settled into an approximately axisymmetric state yet where the rotational energy density has been redistributed. Thus, during this time the thermal energy is not yet affected by the indirect influence of matter redistribution due to centrifugal forces.

This also means that we should be able to observe higher temperatures for higher bulk viscosities during this time because all configurations have a similar compactness as can be observed in Fig. 5, where all configurations have a comparable maximum rest-mass density at $t - t_{\text{mer}} \approx 4.22$ ms. Indeed, we observe that the temperature distributions shown in the top row of Fig. 7 look more homogeneous and feature less “cold” material, i.e., $T \lesssim 5$ MeV, if the bulk viscosity is large. Two effects are important in order to understand this behaviour. First, as already mentioned, higher bulk viscosities lead to more dissipation of kinetic into thermal energy which leads to an increase in temperature if the fluid is not expanding simultaneously (adiabatic cooling might dominate the temperature evolution at a later stage). Second, the decrease in kinetic energy is affecting the redistribution and ejection of loosely bound matter through shock waves. This means that in addition to the dissipative heating due to bulk viscosity the HMNS is also less efficient in transporting heated matter through shock waves. Both of these effects lead to the relatively homogeneous distribution of temperature in the outer layers of the HMNS for the high-viscosity case shown in the top right panel of Fig. 7.

In addition, the lower row shows how the bulk-viscous pressure is distributed. First, given that ρ_l marks the value of the rest-mass density below which we set $\zeta = \zeta_l = 0$, e.g., see Eq. (45), we observe that the bulk-viscous pressure Π be-

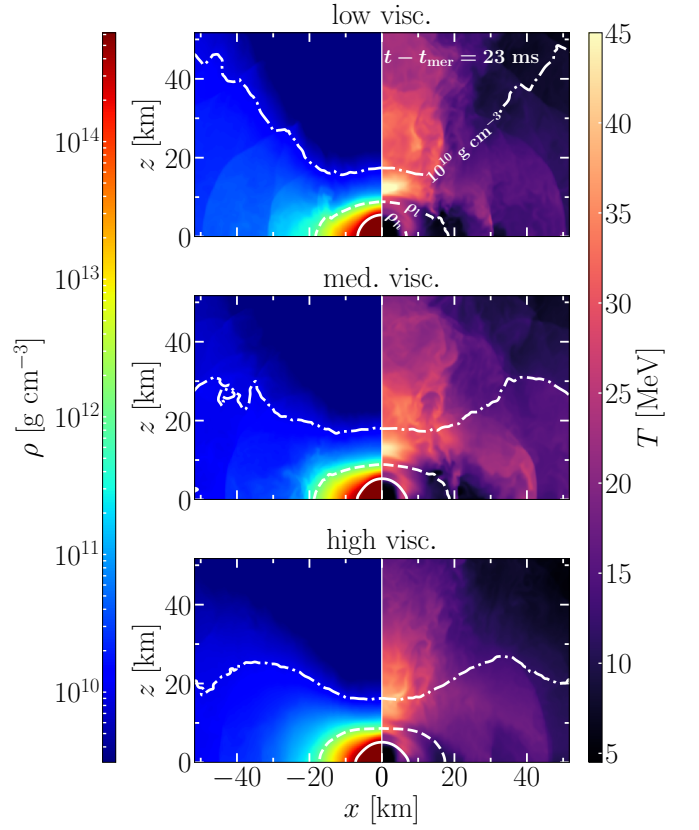


FIG. 8. *Left half:* Cross-sections of the rest-mass density in the (x, z) plane at $y = 0$. The snapshots are taken at $t - t_{\text{mer}} = 23$ ms. Shown is the low viscosity case in the top panel, the medium-viscosity case in the middle panel and the high-viscosity case in the bottom panel. The solid line denotes a density contour at $\rho = \rho_h$, the dashed line denotes a density contour at $\rho = \rho_l$ and the dash-dotted line denotes a low density contour at $\rho = 10^{10} \text{ g cm}^{-3}$. *Right half:* Same as *left half* but for the temperature.

comes vanishingly small for densities below ρ_l . Furthermore, we observe that $|\Pi|/p$ reaches its maximum value in the transition zone $\rho_l < \rho < \rho_h$, i.e., between the dashed and the solid line. The largest values of $|\Pi|$ are reached in regions with densities higher than ρ_h because these regions have the largest oscillations and bulk viscosities. Nevertheless, the largest values of $|\Pi|/p$ are sensitive to the rapid decrease in pressure in the outer layers of the HMNS which is the reason for $|\Pi|/p$ reaching its maximum for $\rho < \rho_h$. Note that, in contrast to the constant bulk-viscosity prescription applied in this work, a microphysical model leads to distributions of $|\Pi|/p$ which are highly sensitive to the temperatures achieved in the HMNS [47].

We also observe that even though the distributions of Π/p are subject to different density oscillations, overall, larger bulk viscosities lead to larger bulk-viscous pressures as one would intuitively expect. We recall that this was not the case for the viscous migration test reported in Fig. 3 as the high-viscosity case was extremely efficient in the damping of density oscillations leading to non-monotonic behaviour in the late evolution.

Last but not least, the distributions of Π/p resemble quadrupolar structures for $\rho_h < \rho$ for all cases. This can be explained by considering the $m = 2$ bar-mode deformation of the HMNS and its interaction with the surrounding matter. It is useful to recall that $\Pi \sim -\zeta\Theta$ in our simulations. This means that regions with $\Pi < 0$ are expanding while regions with $\Pi > 0$ are compressing. First, we observe that one of the intersections between negative and positive bulk-viscous pressure is connecting the two temperature “hot spots” [90] which also correspond to the two largest eddies that developed during the merger. Then, the other intersection separating negative and positive Π regions is found approximately orthogonal to the first intersection connecting the hot spots. As the HMNS is rotating counter-clockwise in Fig. 7 we observe that the regions of the HMNS which are located immediately above either of the two hot spots are always compressing (positive Π) while the regions below either of the two hot spots are expanding (negative Π). As the two eddies located at the two temperature hot spots have the same orientation as the rotation axis of the HMNS, i.e., both rotate counter-clockwise, matter above the hot spots must have a positive Π and matter below a negative Π . The reason for this is that the rotating motions of the eddies compress matter in front of them because of the drag towards the HMNS which means that its density is increasing. Correspondingly, matter behind the eddies expands because of the drag away from the HMNS which means that its density is decreasing.

Finally, in Fig. 8 we discuss sections of the rest-mass density distribution (left half panels) and the distribution of the temperature (right half panels) in the (xz) plane ($y = 0$) at $t - t_{\text{mer}} \approx 23$ ms for the low (top panel), medium (middle panel) and high viscosity (bottom panel) cases. The solid line denotes a density contour at $\rho = \rho_h$, the dashed line denotes a density contour at $\rho = \rho_l$ and the dash-dotted line denotes a low density contour at $\rho = 10^{10} \text{ g cm}^{-3}$. This figure helps us to understand the impact of large bulk viscosities on the overall structure of the long-lived HMNS and torus when a quasi-stationary state is reached. First, we observe that the torus has a smaller extent, if the bulk viscosity is increased. Also, the HMNS has a less oblate shape with larger bulk viscosities which is related to the less efficient angular momentum transport to the outer layers of the remnant. In general, large bulk viscosities prevent neutron star matter from reaching large radii which leads to an overall more compact envelope and an higher concentration of angular momentum at smaller radii.

Second, focussing on the temperature distributions, we find that the low density funnel above the HMNS has overall lower temperatures with larger bulk viscosities. At this point it is important to remark that large temperatures in the funnel region are most likely the consequence of using a hybrid EOS with an ideal gas law because a comparable study using fully tabulated hot EOSs did not show this behaviour [58]. However, since we are interested in learning about the qualitative impact that large constant bulk viscosities have in the post-merger phase, it is still interesting to compare the temperature distributions for the different cases in order to understand how bulk viscosity can possibly impact the funnel region. In our

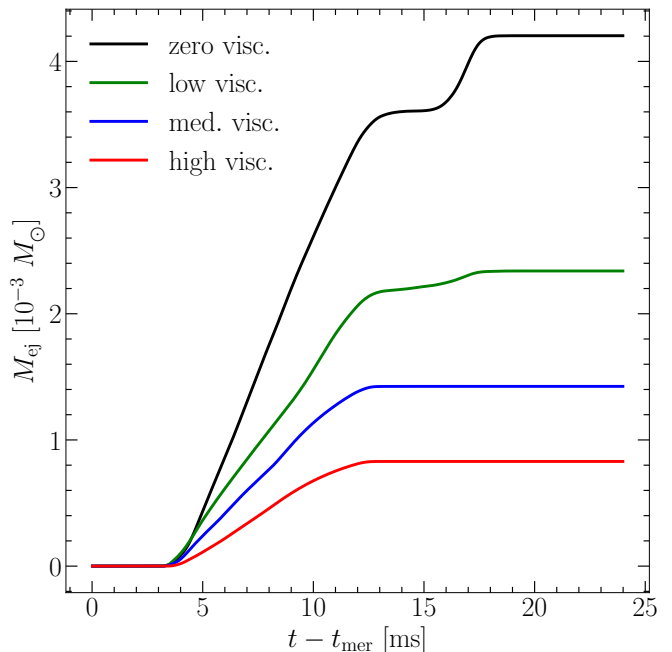


FIG. 9. Cumulative ejected mass from the Bernoulli criterion for the zero (black line), low (green line), medium (blue line) and high (red line) viscosity case. The detector is placed at ~ 517 km for all viscosity cases.

case, large temperatures in the funnel region stem from bound shock-heated material which accumulates above the HMNS. As bulk viscosity tends to damp violent nonlinear density oscillations of the HMNS, which are a primary source of shock waves, larger bulk viscosities tend to produce weaker shock waves and therefore less efficient shock-heating in the funnel region.

3. Dynamical mass ejection

In this subsection we discuss the impact of large bulk viscosities on the dynamical mass ejection in our simulations. We start by showing the total unbound material passing through a detector at ~ 517 km and calculated by using the Bernoulli criterion, i.e., material is classified as being unbound if $-hu_t - h_\infty > 0$ with h_∞ being the minimum specific enthalpy of the cold EOS table employed, see also [91]. Figure 9 shows the cumulative unbound mass as a function of $t - t_{\text{mer}}$ for all viscosity cases. We observe a clear impact of bulk viscosity on the total unbound material. Large bulk viscosities suppress dynamical mass ejection. For the high-viscosity case the total ejecta mass is only $\sim 20\%$ of the mass measured for the zero-viscosity case.

Figure 10 shows the velocity distribution of the total unbound material at the end of the simulations for all viscosity cases. The impact of bulk viscosity on the velocity distributions is less severe than its impact on the ejected mass. We observe that large bulk viscosities tend to suppress ejecta with velocities below ~ 0.2 and above ~ 0.5 compared to the less

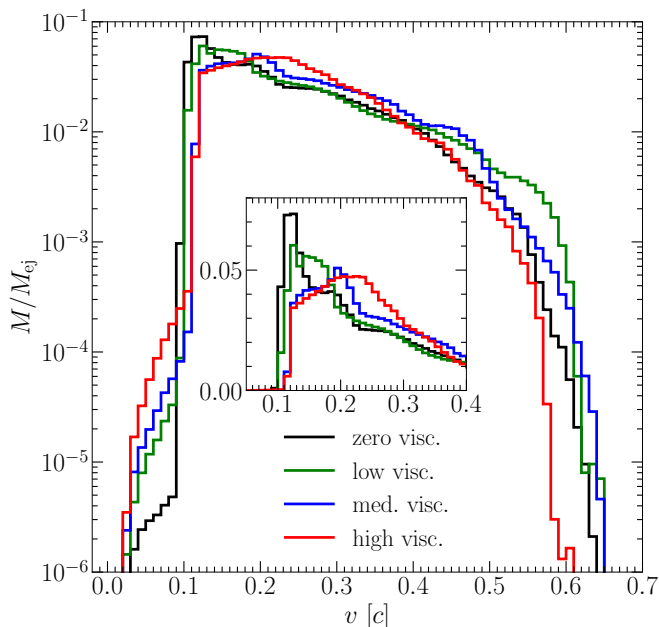


FIG. 10. Velocity distribution of the ejected mass with $v = \sqrt{v_i v_i}$ at the end of our simulations for the zero (black line), low (green line), medium (blue line) and high (red line) viscosity case. The inset shows a zoom-in around the mean of the distribution. The detector is placed at ~ 517 km for all viscosity cases.

viscous cases. Therefore, as can be seen from the inset in Fig. 10, the median of the distribution tends to shift to higher velocities. We suspect that the slow ejecta, more precisely, ejecta with $v \lesssim 0.2$, observed in the zero and low viscosity cases stems from marginally unbound material which is accelerated by shock waves which pass through it. Large viscosities would naturally suppress this type of ejecta due to less efficient shock-heating, see also the discussion of Figs. 7 and 8. As a consequence, the distribution of the ejecta in v shifts to higher velocities as only the marginally unbound material with low velocities is affected by this mechanism. The suppression of the *fast* ejecta component is the direct result of strong viscous damping of early density oscillations. The fast ejecta component originates from the first bounces of the two neutron star cores. As bulk viscosity tends to damp these violent collisions most efficiently, the energy reservoir powering the ejection of fast matter is dissipated and leads to a reduction of fast unbound matter.

Next, we will discuss the geometric distribution of the dynamical ejecta. Figure 11 shows the rest-mass density (top half panels) and the quantity $-h v_t - h_\infty$ (bottom half panels) at $t - t_{\text{mer}} \approx 7.11$ ms for all configurations in the equatorial plane. We observe that an increase in bulk viscosity leads to a more asymmetric shape of the outermost ejecta front which is at the same time a major component of the overall dynamical ejecta. This means that large bulk viscosities tend to select a preferred direction of the dynamical ejecta in the ϕ -direction. In our case, mass ejection tends to be increased for the angles $\phi \approx \pi/4$ and $\phi \approx 5\pi/4$. This finding is further supported by the Mollweide projections of the normalized surface den-

sity as calculated from the cumulative ejected mass per solid angle presented in Fig. 12. Solid lines denote contour lines at $8 \times 10^{-7} M_\odot^{-2}$. For the medium and high-viscosity case we observe pockets of low mass ejection in the equatorial plane with less than $8 \times 10^{-7} M_\odot^{-2}$. On the other hand, we also observe that the medium and high-viscosity cases tend to reach higher densities inside the contour lines.

This effect can easily be explained by considering that the dynamical ejecta consists of a tidally ejected component and a shock-heated component [92]. The tidally ejected component is weakly affected by bulk viscosity in our simulations as we set $\zeta = 0$ in low density matter which is more likely to get unbound through tidal forces. In contrast, as already explained above together with Fig. 8, strong bulk viscosities reduce shock-heating. Hence, the first bounce of the two neutron star cores powers significantly more matter ejection than all subsequent bounces, if the bulk viscosity is large. Therefore, matter is ejected primarily in the direction of the first bounce for the high-viscosity case, while for the cases with a lower viscosity matter, ejection from the subsequent core bounces tends to be more symmetric along the ϕ -direction. Furthermore, from Fig. 12 we observe only a weak influence of bulk viscosity on the surface density distribution in the θ -direction. In the contrast to the ϕ -direction, the surface density in the high-viscosity case is more uniform along θ for a given ϕ than in the low viscosity case. Thus, while large bulk viscosities increase the degree of anisotropy of the outflow in the ϕ -direction, they also show a weak tendency to decrease anisotropy in the θ -direction.

To conclude this subsection, we present in Fig. 13 the same quantities as in Fig. 8 focussing now, however, on the distributions at large distances from the HMNS. Additionally, we present another low density contour at $\rho = 10^8 \text{ g cm}^{-3}$ using a dotted lines in order to visualize the envelope or torus. We find that large bulk viscosities lead to a significantly more compact envelope or torus as can be seen from the size of the different areas enclosed by the dotted line. We attribute this observation to the less efficient transport of matter to large distances which is a direct effect of large bulk viscosities. The temperature distributions at large distances are comparable for all cases which indicates that the impact of bulk viscosity on the thermal properties of matter located in the torus is weak.

IV. CONCLUSIONS

We present a comprehensive report about the impact of a constant bulk viscosity on BNS mergers using numerical simulations where dissipative effects are included self-consistently through the causal and second-order formulation by MIS. In the interest of exploring the most elementary scenario, we make use of a particularly simplified microphysical model for the bulk viscosity where it assumes a constant value within the neutron stars and is set to zero below a certain threshold density. This approach is simpler than the one carried out in Ref. [47], where the transport coefficients arise consistently from microphysical arguments leading to complex functions of density and temperature. At the same time,

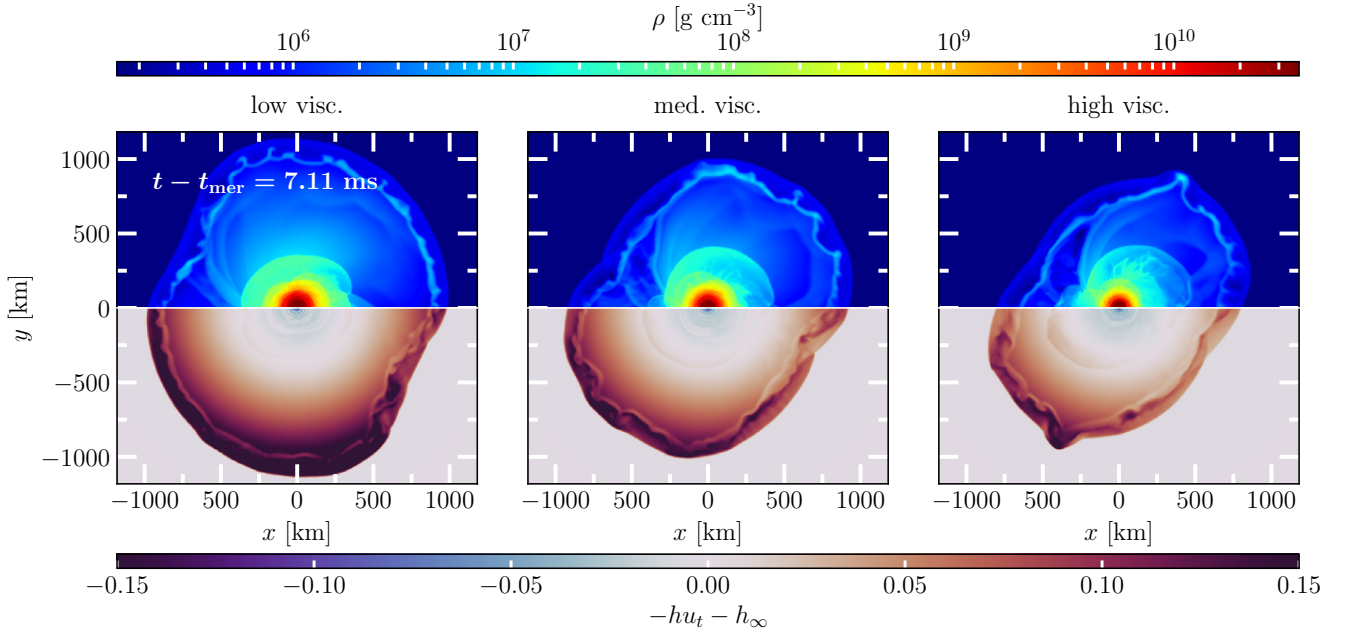


FIG. 11. *Top half*: Cross-sections of the rest-mass density in the (x, y) plane at $z = 0$. The snapshots are taken at $t - t_{\text{mer}} = 7.11 \text{ ms}$. Shown is the low viscosity case in the left panel, the medium viscosity case in the middle panel and the high viscosity case in the right panel. *Bottom half*: Same as *top half* but for the Bernoulli criterion.

the simpler approach presented here has the important advantage of being independent of the EOS and thus more suitable for serving as a numerical testbed.

First, we present a detailed description of the numerical methods used in [47] and of the numerical tests performed in order to verify our implementation. Most notably, we employ a modified version of the inversion algorithm proposed in [81], where several limiting procedures ensure causality of the evolution, as well as existence and uniqueness properties of the root-finding function used in the conversion between conservative and primitive variables.

As a first test case we consider the measurement of numerical viscosity and calculate the damping time of the radial fundamental eigenmode of an isolated TOV solution with bulk viscosity. By evolving stars with different physical bulk viscosities and different resolutions we were able to observe that the measured bulk viscosity asymptotes to a constant value for high resolutions. The measured asymptotic value differs at most by $\lesssim 35\%$ from the physical input viscosity which is a reasonable agreement considering the strong approximations used in the measurement procedure. Additionally, we find that the convergence order of our code is strongly affected by the relative importance of discretization errors originating from the ill-balanced surface or the smooth interior. In a representative setup we obtained numerical viscosities $\lesssim 10^{26} \text{ g cm}^{-1} \text{ s}^{-1}$ which is a promising finding considering that realistic viscosities reach values of $\gtrsim 10^{27} \text{ g cm}^{-1} \text{ s}^{-1}$ [41, 93] in isolated stars and BNS mergers.

As a second test case we simulate the violent migration of unstable neutron stars to the stable branch. In contrast to the first test case, this scenario tests the implemented equations

in a nonlinear regime. We observe that dissipative heating leads to a decrease of the central rest-mass density because the contribution of the thermal pressure in the neutron star core increases. The contribution can reach values of up to $\sim 10\%$ of the total pressure for the highest viscosity case. Additionally, this test case allows us to provide evidence that our scheme is able to handle the transition between a viscous neutron star and an inviscid low density exterior. This is an important ability as it allows us to study the impact of bulk viscosity on mass ejection in BNS merger simulations. We show that shock waves which originate at the neutron star surface located in viscous matter propagate without any numerical disturbance through the transition region between viscous and inviscid matter. This allows us to observe that higher viscosities lead to weaker shock waves in the second and third bounce during migration. It is due to the efficient dissipation of kinetic energy into heat that a lower amount of energy is transferred to the shock wave for higher bulk viscosities.

Finally, we explore BNS simulations with a constant bulk viscosity. We report on thermal and structural properties of the HMNS remnant, as well as the impact of bulk viscosity on dynamical mass ejection. We find that for large viscosities, the increase of the total thermal energy due to dissipative heating is counteracted by the lower density of the HMNS core. These lower densities are the result of the additional centrifugal support in the HMNS core observed. It is important to remark that when dropping the assumption of constant bulk viscosity and adopting instead a microphysical model for the latter, leads to a denser and more compact remnant due to the strong temperature dependence of the microphysical bulk viscosity [47].

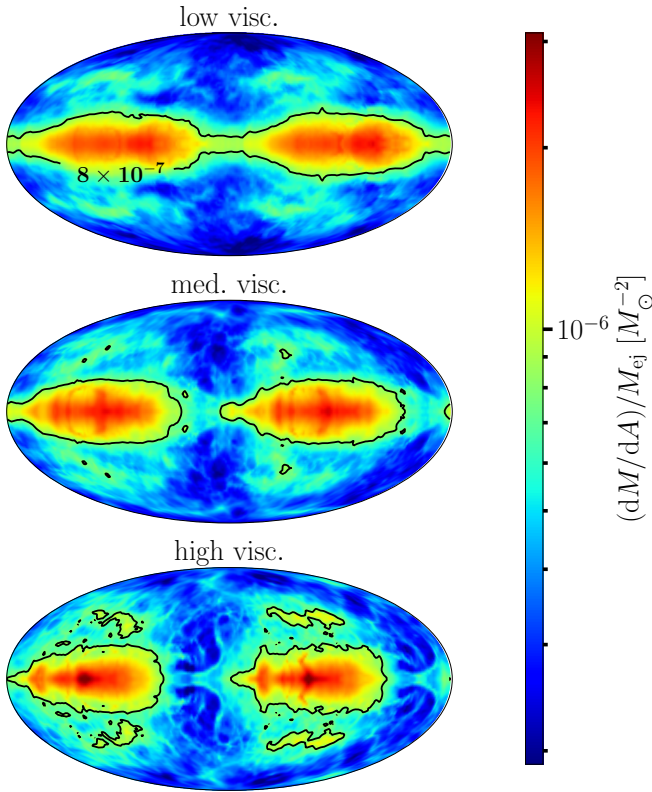


FIG. 12. Mollweide projections of the surface density as calculated from the cumulative ejected mass per solid angle measured by using the Bernoulli criterion at the end of our simulations. The values are normalized by the corresponding total mass of the ejecta. The detector surface is placed at ~ 517 km. Shown is the low viscosity case in the top panel, the medium-viscosity case in the middle panel and the high-viscosity case in the bottom panel. Solid lines denote contour lines at $8 \times 10^{-7} M_{\odot}^{-2}$.

We also observe a more uniform temperature distribution and less efficient shock-heating in the HMNS remnant. We attribute this behaviour to the dissipation of kinetic energy into heat and, as a result, a less efficient kinetic-energy transfer from the fast-rotating deformed HMNS core to the matter making up its envelope. Furthermore, we measure inverse Reynolds numbers on the order of $\sim 1\%$ in the center of the HMNS directly after the merger for the highest viscosity considered. This corresponds to bulk-viscous pressures, which are approximately $\sim 20\%$ of the total EOS pressure. Overall, the remnant of a viscous BNS merger has a significantly smaller torus and at the same time a less dense core.

Finally, the dynamical mass ejection from viscous BNS mergers is in agreement with the overall results presented so far. We find that the dynamically ejected mass in our simulations is suppressed by a factor of approximately five for the high-viscosity case when compared to the inviscid case. Again, this is the result of efficient dissipation of kinetic energy which makes it hard to unbind mass. Interestingly, we also find that the distribution of ejected matter along the azimuthal direction becomes more anisotropic with increasing

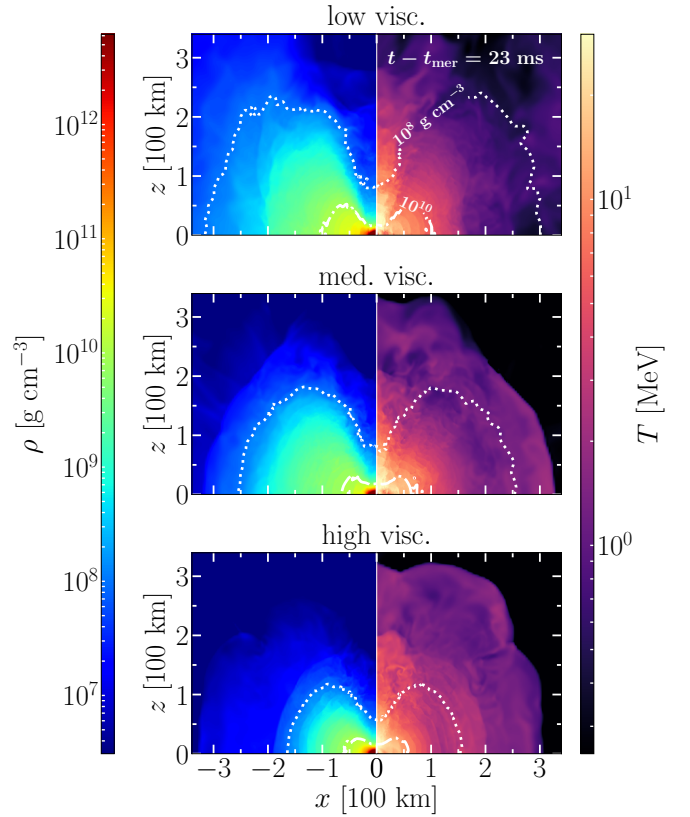


FIG. 13. Same as Fig. 8 but for a much larger domain focussing on the envelope of the remnant. Note that we present an additional low density contour at $\rho = 10^8 \text{ g cm}^{-3}$ by using a dotted line and that the colorbars have a different scale.

viscosities. We attribute this behaviour to the fact that for large viscosities most of the unbound material stems from the first collision-and-expansion cycle of the two stars. Thus, matter is ejected in a preferred direction.

ACKNOWLEDGMENTS

It is a pleasure to thank M. Alford, M. Hanauske, E. Most, and K. Schwenzer for useful comments and discussions. Partial funding comes from the GSI Helmholtzzentrum für Schwerionenforschung, Darmstadt as part of the strategic R&D collaboration with Goethe University Frankfurt, from the State of Hesse within the Research Cluster ELEMENTS (Project ID 500/10.006), by the ERC Advanced Grant “JETSET: Launching, propagation and emission of relativistic jets from binary mergers and across mass scales” (Grant No. 884631) and the Deutsche Forschungsgemeinschaft (DFG, German Research Foundation) through the CRC-TR 211 “Strong-interaction matter under extreme conditions” – project number 315477589 – TRR 211. LR acknowledges the Walter Greiner Gesellschaft zur Förderung der physikalischen Grundlagenforschung e.V. through the Carl W. Fueck Laureatus Chair. The simulations were performed on HPE Apollo HAWK at the High Performance Computing Center Stuttgart (HLRS)

under the grant BNSMIC.

Appendix A: Measurement procedure

Following [83] and [94] the rate of change of the kinetic energy of a weakly pulsating star, i.e., the magnitude of the pulsation is small such that linear perturbation theory is applicable, is given by

$$\frac{dE}{dt} = -4\pi \int_0^R dr r^2 \sqrt{-g} \zeta |\Theta|^2, \quad (\text{A1})$$

where g is the determinant of the spacetime metric $g_{\mu\nu}$ and R is the radius of the neutron star. Then, if the pulsation energy E is known, the damping time of density and velocity perturbations $\bar{\tau}$ can be simply estimated through

$$\bar{\tau} = -2E \left\langle \frac{dE}{dt} \right\rangle^{-1}, \quad (\text{A2})$$

where $\langle \cdot \rangle$ denotes the time-average over one pulsation period. It is interesting to note that a similar formula can be derived from the simple damped harmonic oscillator by assuming that $\bar{\tau} \gg 2\pi\omega^{-1}$, where ω is the angular frequency of the corresponding undamped case.

Truncating E and dE/dt at leading order in the post-Newtonian expansion, see [83] for details, we obtain the following expressions

$$E = 4\pi \int_0^R dr r^2 \sqrt{-g} \frac{1}{2} \rho_B v'^2, \quad (\text{A3})$$

$$\frac{dE}{dt} = -4\pi \int_0^R dr r^2 \sqrt{-g} \zeta |\Theta|^2, \quad (\text{A4})$$

where $v' = v - v_B = v$ is the Newtonian three-velocity perturbation in the radial direction with v_B being the background velocity. The background velocity is set to zero in our case, i.e., $v_B = 0$. Analogously, ρ_B is the background density profile of the TOV solution.

Assuming a harmonic form of the perturbation, i.e., $v' \propto \exp[i\omega t + ikr]$, where k is the wavenumber, we obtain

$$\langle |\Theta|^2 \rangle \propto k^2 \langle v'^2 \rangle = k^2 v_{\text{max}}'^2 / 2. \quad (\text{A5})$$

The quantity v_{max}' is a function of radius. Analogously to the simple harmonic oscillator, the energy oscillates between kinetic and potential energy. Therefore E can be estimated by substituting v_{max}' for v' . Then, by using the definition of the speed of sound $c_s^2 = \omega^2/k^2$ and assuming ζ to be constant within the star we obtain

$$E = 2\pi \int_0^R dr r^2 \sqrt{-g} \rho_B v_{\text{max}}'^2, \quad (\text{A6})$$

$$\left\langle \frac{dE}{dt} \right\rangle \sim -2\pi \frac{\omega^2}{c_s^2} \zeta \int_0^R dr r^2 \sqrt{-g} v_{\text{max}}'^2. \quad (\text{A7})$$

Finally, by using Eq. (A2) we find a formula which relates the damping time of radial pulsations $\bar{\tau}$ to the bulk viscosity ζ

$$\zeta = \frac{2}{\bar{\tau}} \frac{c_s^2}{\omega^2} \bar{\rho}, \quad (\text{A8})$$

where

$$\bar{\rho} := \frac{\int_0^R dr r^2 \sqrt{-g} v_{\text{max}}'^2 \rho_B}{\int_0^R dr r^2 \sqrt{-g} v_{\text{max}}'^2}, \quad (\text{A9})$$

is the eigenmode-averaged background density. In practice, ω can be obtained from the simulations by measuring the pulsation frequency, $\bar{\rho}$ can be obtained from the initial data by calculating the integrals in Eq. (A9) and c_s^2 can be simply evaluated at $\bar{\rho}$ by using the polytropic part of the EOS, i.e.,

$$c_s^2 = \left[\frac{1}{\Gamma \kappa \bar{\rho}^{\Gamma-1}} + \frac{1}{\Gamma - 1} \right]^{-1}. \quad (\text{A10})$$

This means that we are left with the determination of $\bar{\tau}$ in order to calculate ζ through Eq. (A8).

As already mentioned above, we use the central density ρ_c to measure the damping time $\bar{\tau}$. In order to do so, we make use of the following simple recipe:

1. *Use a high-order low-pass Butterworth filter in order to remove global drifts of the central density from the signal.*

As can be seen from the left panel of Fig. 14, our simulations have a typical length on the order of $\sim \mathcal{O}(100 \text{ ms})$ which yields a minimum resolved frequency of $f_{\text{min}} \sim 0.01 \text{ kHz}$. We choose the cutoff-frequency on the order of $f_c \sim 0.1 \text{ kHz}$ and a $n = 4$ filter, where n denotes the order of the Butterworth filter. The frequency of the fundamental mode is $f_F \sim 1.44 \text{ kHz}$, see e.g., [84], which means that our cutoff-frequency is more than an order of magnitude lower than the frequency we want to resolve. Thus, the choices $f_c \sim 0.01 \text{ kHz}$ and $n = 4$ ensure that we obtain the density drift without contributions from higher frequencies. Then, we subtract the drift from the original data and obtain a signal which oscillates around zero. Afterwards, we normalize the signal by the initial central density $\rho_{c,0}$. We define the “drift-free” and normalized signal as $\delta\rho$ which is shown in the left panel of Fig. 14 in solid thin lines for the simulations with the highest resolution.

2. *Calculate the local maxima of the signal.*

Assuming that the signal is composed of a sum of damped sinusoids, we can calculate the local maxima of the signal in order to obtain data which can be fitted to a simple exponential function. The main caveat in this approach is that it is not possible to distinguish between different excitation modes with different damping times. This means that it is necessary select only those parts of the timeseries of $\delta\rho$ which are dominated by a single eigenmode; the fundamental or F -mode in

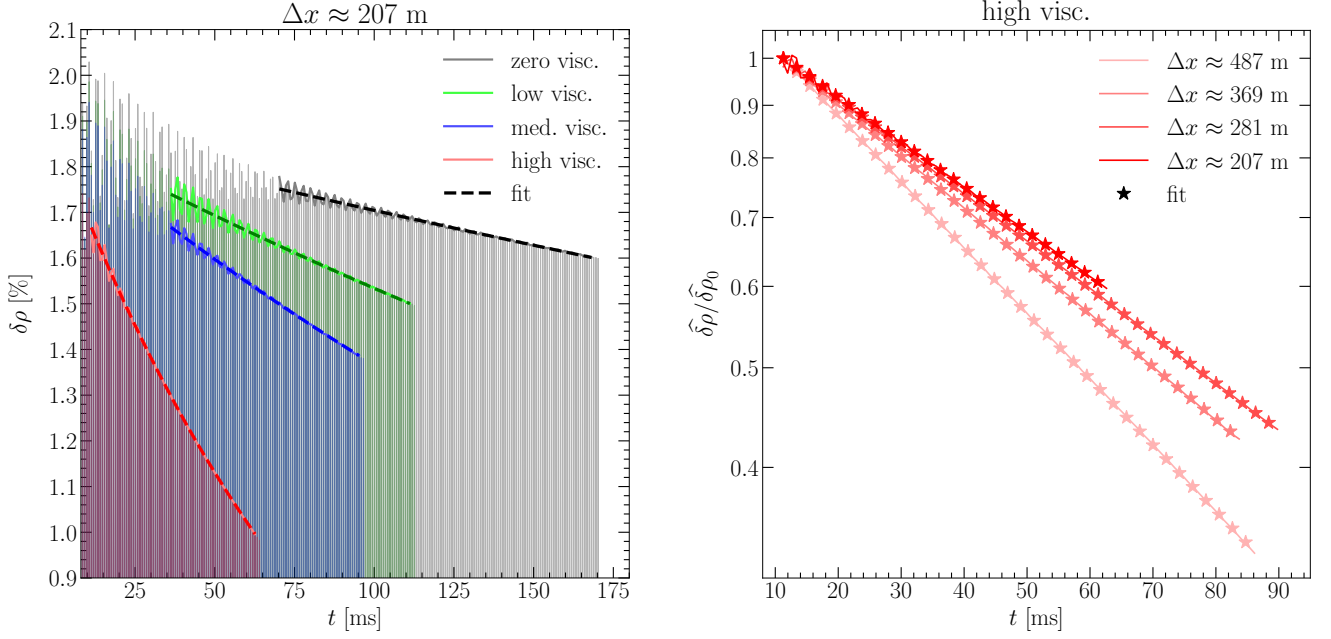


FIG. 14. *Left*: Shown in solid thin lines is the timeseries of the normalized central density for the zero (black line), low (green line), medium (blue line) and high (red line) viscosity case, where the density drift has been removed from the data. Shown in solid thick lines is the corresponding envelope of $\delta\rho$ estimated by using the local maxima of the signal. Note that the envelopes start at $t \neq 0$ indicating that data before the starting point has been discarded. Corresponding dashed lines denote fits to the envelope of $\delta\rho$. Overall, we show only data for the highest resolution, i.e., $\Delta x \approx 207$ m. *Right*: Solid lines show the timeseries of the local maxima of $\delta\rho$ normalized by its first value. We show only data for the high-viscosity case but for all employed numerical resolutions by using different shades of red. Higher resolutions are represented by a darker shading. The star symbols denote fits to $\hat{\delta\rho}/\hat{\delta\rho}_0$.

our case. This is not a problem for lower resolution simulations as the overtone modes have a shorter damping time due to more efficient numerical damping.

Therefore, for lower resolution simulations the contamination of the signal is reduced such that almost all of $\delta\rho$ is dominated by the F -mode. However, as numerical damping decreases with increasing resolution also the contributions from excited overtone modes become non-negligible. This can be seen in the left panel of Fig. 14 where for $t \lesssim 50$ ms the evolution of the local maxima is highly oscillatory due to contributions from overtone modes. A naive computation of the local maxima together with a subsequent fitting procedure results in an underestimation of $\bar{\tau}_F$ because overtone modes have shorter damping times than the fundamental mode. Thus, for higher resolution simulations we make only use of approximately the last half of the signal where the contributions from the overtone modes can be neglected. We show thick solid lines which connect the local maxima in the left panel of Fig. 14 in order to visualize the utilised part of $\delta\rho$. The timeseries of the utilised local maxima of $\delta\rho$ is defined as $\hat{\delta\rho}$ and the first value in this sequence is defined as $\hat{\delta\rho}_0$.

3. *Fit the logarithm of the local maxima to a linear function in time.*

In this step we additionally normalize $\hat{\delta\rho}$ by $\hat{\delta\rho}_0$ and fit

the values of $\log[\hat{\delta\rho}/\hat{\delta\rho}_0]$ to a linear function in time. The results are shown in the left and right panels of Fig. 14. Dashed lines in the left panel of Fig. 14 and the star symbols in right panel of Fig. 14 represent the fits, respectively. To avoid overcrowding the right panel of Fig. 14, we only show $\hat{\delta\rho}/\hat{\delta\rho}_0$ for the high-viscosity case. Different color intensities in the right panel of Fig. 14 show different resolutions and solid lines connect the original data points of $\hat{\delta\rho}/\hat{\delta\rho}_0$.

From the right panel of Fig. 14 we observe convergent behaviour in the slopes of the linear fits. This is expected because increased numerical resolution leads to a decrease of the numerical viscosity such that the measured damping time converges to the damping time related to the physical viscosity. Finally, we observe oscillatory behaviour in the data presented for the highest resolution in the right panel of Fig. 14. As already discussed, these oscillations stem from contributions of overtone modes and do not significantly impact the calculation of $\bar{\tau}_F$.

Appendix B: Convergence

Because of the reduced convergence order found in Fig. 2 it is interesting to compare to another numerical viscosity measurement performed during an earlier development stage

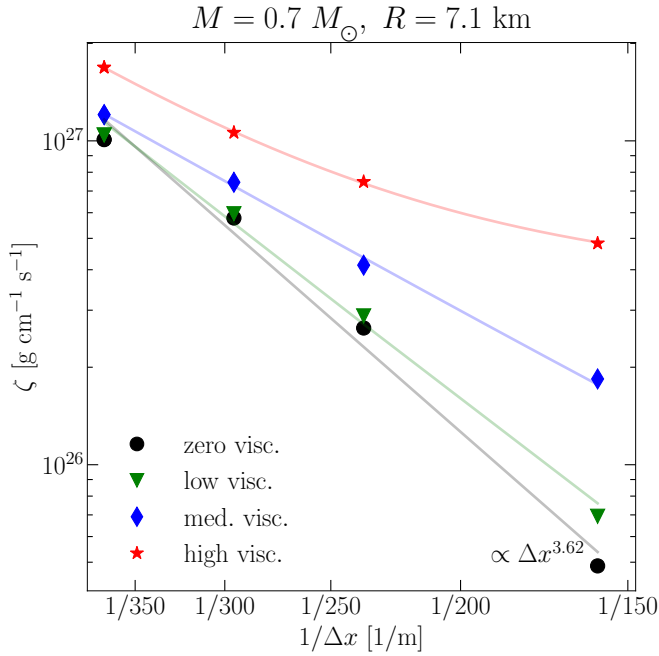


FIG. 15. Same as Fig. 2 but for a TOV solution with a smaller mass and radius.

of our bulk-viscous extension of FIL. In that case, we employed a different TOV solution where $\kappa = 25$, $\Gamma_{\text{th}} = 2$ and $\rho_c = 5.12 \times 10^{-3} M_\odot^{-2} \approx 3.16 \times 10^{15} \text{ g cm}^{-3}$. All other parameters of the EOS are the same. This setup yields a $M = 0.7 M_\odot$ star with a $R = 7.1 \text{ km}$ radius. The bulk viscosity is varied between $\zeta_h \in [0, \sim 2.73 \times 10^{25}, \sim 1.64 \times 10^{26}, \sim 5.47 \times 10^{26}] \text{ g s}^{-1} \text{ cm}^{-1}$, which are denoted as zero, low, medium and high-viscosity cases, respectively. The resolution on the finest refinement level varies between $\Delta x \in \{\sim 158, \sim 236, \sim 295, \sim 369\} \text{ m}$. Furthermore, instead of employing the cubic polynomial presented in Eq. (45), ζ is set to zero sharply for $\rho < 2.56 \times 10^{-4} M_\odot^{-2} \approx 1.58 \times 10^{14} \text{ g cm}^{-3}$.

Figure 15 presents the same numerical viscosity measurement as shown in Fig. 2 for the small TOV solution. Table II presents the corresponding fitting coefficients. First, we observe that only for the high-viscosity case the fit shows a concave shape indicating that the low and medium-viscosity cases are dominated by numerical viscosity, even at high resolutions. More importantly, we also find that the convergence order for the zero viscosity case, i.e., ~ 3.62 , is consistent with the formal convergence order of our numerical schemes. This is in contrast to the reduced convergence order of ~ 1.79 found in Fig. 2. We suspect that this behaviour is related to the amount of grid points covering the stars in both cases. For the highest resolution of the setup presented in Fig. 15, the neutron star is covered by only $\sim 66\%$ of the points of the more realistic bigger star simulated at the highest resolution in Fig. 2. This is a direct consequence of the smaller radius of the setup in Fig. 15 which results in a lower effective resolution.

Now, the reduced effective resolution of the setup in Fig. 15 increases the numerical error originating from the interior of

Model	ζ_a	ζ_s	p_h
	$[\text{g s}^{-1} \text{ cm}^{-1}]$	$[\text{g s}^{-1} \text{ cm}^{-1}]$	
zero visc.	—	1.66×10^{33}	3.62
low visc.	—	3.49×10^{32}	3.23
med. visc.	8.87×10^{24}	1.04×10^{31}	2.32
high visc.	3.66×10^{26}	8.29×10^{31}	2.83

TABLE II. Fitting results to the measured bulk-viscosity values presented in Fig. 15 using Eq. (53) with $\lambda \approx 1.74 \times 10^4 \text{ m}$. Note that the values of ζ_a for the zero and low-viscosity case are not available due to the fact that we applied a linear fit of $\log[\zeta]$ as a function of $\log[\Delta x]$ for both cases. Using Eq. (53) for the low-viscosity case resulted in negative values for ζ_a due to the convex shape of the corresponding data points in Fig. 15.

star. Due to the smooth behaviour of the solution in the neutron star interior, the convergence order in this region is expected to be close to the formal one. Hence, we suspect that the setup in Fig. 15 leads to a measured convergence order closer to the formal one because the damping of central density oscillations is dominated by discretization errors which originate from the low effective resolution in the neutron star interior. In contrast, the damping of the zero-viscosity case in Fig. 2 is dominated by discretization errors from the ill-balanced neutron star surface which leads to a deterioration of the convergence order. This is a direct consequence of the larger radius which leads to small discretization errors from the neutron star interior due to a higher effective resolution.

Appendix C: Rotational properties of neutron star mergers with a constant bulk viscosity

The left panel of Fig. 16 reports the evolution of the $m = 2$ density mode, or bar-mode [95]

$$\mathcal{P}_m := \int \rho W e^{-im\phi} \sqrt{\gamma} dx dy dz, \quad m = 2, \quad (\text{C1})$$

when normalized to its value at the time of the merger $\mathcal{P}_{2,0}$, and for the four values of constant bulk viscosity considered in our simulations, see also [47]. Note that the initial oscillations for $t - t_{\text{mer}} \lesssim 3 \text{ ms}$ are the result of the rapid and quasi-periodic collisions of the two stellar cores (see [96] for a mechanical toy model). Furthermore, the evolution of $\mathcal{P}_2/\mathcal{P}_{2,0}$ is impacted in a systematic manner by the strength of the bulk viscosity, which suppresses the $m = 2$ deformation and hence leads to a more axisymmetric HMNS. Note that when moving away from the constant value adopted in this work, a microphysical model for the bulk-viscosity leads to increased bar-deformations [47]. Since the bar-deformation represents a way in which the HMNS minimises its rotational energy [95], it is natural to expect that bulk viscosity will equally impact the rotational properties of the HMNS. We quantify the latter by computing the rotational kinetic energy of the merger remnant [see, e.g., Eq. (12.48) of [52] for a definition].

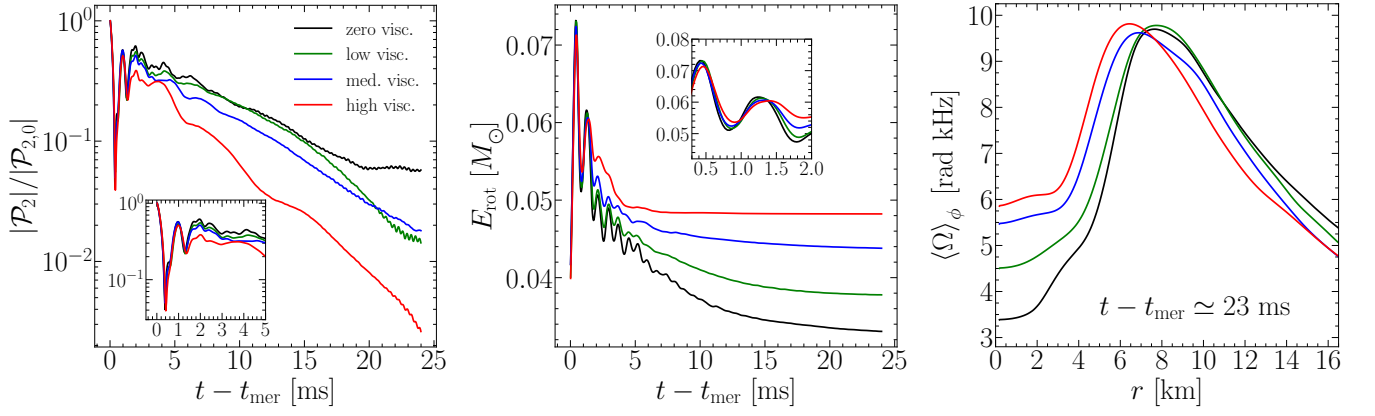


FIG. 16. *Left*: Evolution of the $m = 2$ rest-mass density mode \mathcal{P}_2 normalized to its value at the time of the merger $\mathcal{P}_{2,0}$ for the four constant viscosity cases considered. *Middle*: The same as on the left but for the rotational kinetic energy. *Right*: ϕ -averages in the equatorial plane of the angular velocity as a function of the coordinate radius r at a representative late times ($t - t_{\text{mer}} \approx 23$ ms).

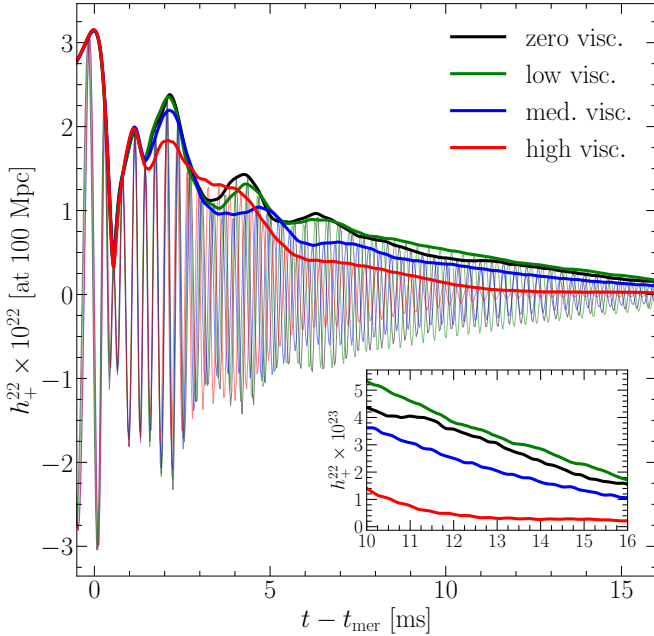


FIG. 17. GW strain in the $\ell = m = 2$ mode of the $+$ -polarization extracted at ~ 740 km and normalized to a distance of 100 Mpc for the four configurations considered. Thick solid lines report the corresponding amplitudes.

The middle panel of Fig. 16 reports the evolution of the rotational energy. We observe that the late-time rotational energy depends on the strength of the bulk viscosity, with larger bulk viscosities leading to a higher E_{rot} ¹. To under-

stand this result it is sufficient to bear in mind that by removing non-axisymmetric deformations, bulk viscosity is effectively quenching GW emission and hence conserving the (rotational) energy of the HMNS.

Further evidence for this dynamics is provided in the right panel of Fig. 16, which shows the azimuthal (ϕ) averages in the equatorial plane of the angular velocity as a function of the coordinate radius r at a representative late time, i.e., $t - t_{\text{mer}} \approx 23$ ms (time averages over 2 ms yield very similar profiles). While this is appreciable already early in the post-merger evolution, i.e., at $t - t_{\text{mer}} \lesssim 5$ ms, the right panel of Fig. 16 clearly shows that the angular velocity of the HMNS core (left panel), i.e., for $r \lesssim 8$ km is larger in the case of large bulk viscosities and after reaching a local maximum at $\approx 4 - 5$ km, it falls off following a Keplerian profile. In turn, the larger centrifugal and thermal support available in the central regions of the HMNS with large viscosities changes the stellar structure and leads to progressively smaller values of the rest-mass density in the core of the HMNS, see left panel of Fig. 5, and to larger values in the envelope (not shown); as a result, the peak of the angular velocity moves inwards with increasing bulk viscosity.

Overall, by comparing our simulations in this work, which employ a constant bulk viscosity within the neutron stars, with those utilizing a model based on realistic microphysical arguments [47] we observe an “inverted” behaviour of \mathcal{P}_2 as described above. As a result, GW emission is decreased instead of increased such that the rotational properties of the HMNS remnant are altered towards larger rotational energies and less compact remnants. We support this point of view by reporting the post-merger GW signal in Fig. 17.

¹ A non-monotonic behaviour is observed for the late-time evolution of \mathcal{P}_2 in the cases of $\zeta = 0.2\zeta_0$ and $\zeta = 0.5\zeta_0$; this is not particularly surprising given that the differences in viscosity are comparable with the fluctuations

introduced by the turbulent motion of the fluid (see also [58] for a similar behaviour).

-
- [1] B. P. Abbott, R. Abbott, T. D. Abbott, F. Acernese, K. Ackley, C. Adams, T. Adams, P. Addesso, R. X. Adhikari, V. B. Adya, and et al. (LIGO Scientific Collaboration and Virgo Collaboration), Gw170817: Observation of gravitational waves from a binary neutron star inspiral, *Phys. Rev. Lett.* **119**, 161101 (2017), [arXiv:1710.05832 \[gr-qc\]](#).
- [2] M. R. Drout, A. L. Piro, B. J. Shappee, C. D. Kilpatrick, J. D. Simon, C. Contreras, D. A. Coulter, R. J. Foley, M. R. Siebert, N. Morrell, K. Boutsia, Z. Wan, and D. D. Whitten, Light curves of the neutron star merger GW170817/SSS17a: Implications for r-process nucleosynthesis, *Science* **358**, 1570 (2017), [arXiv:1710.05443 \[astro-ph.HE\]](#).
- [3] P. Cowperthwaite *et al.*, The electromagnetic counterpart of the binary neutron star merger ligo/virgo gw170817. ii. uv, optical, and near-infrared light curves and comparison to kilonova models, *Astrophys. J. Lett.* **848**, L17 (2017).
- [4] E. Annala, T. Gorda, A. Kurkela, and A. Vuorinen, Gravitational-Wave Constraints on the Neutron-Star-Matter Equation of State, *Phys. Rev. Lett.* **120**, 172703 (2018), [arXiv:1711.02644 \[astro-ph.HE\]](#).
- [5] A. Bauswein, O. Just, H.-T. Janka, and N. Stergioulas, Neutron-star Radius Constraints from GW170817 and Future Detections, *Astrophys. J. Lett.* **850**, L34 (2017), [arXiv:1710.06843 \[astro-ph.HE\]](#).
- [6] B. Margalit and B. D. Metzger, Constraining the Maximum Mass of Neutron Stars from Multi-messenger Observations of GW170817, *Astrophys. J. Lett.* **850**, L19 (2017), [arXiv:1710.05938 \[astro-ph.HE\]](#).
- [7] D. Radice, A. Perego, F. Zappa, and S. Bernuzzi, GW170817: Joint Constraint on the Neutron Star Equation of State from Multimessenger Observations, *Astrophys. J. Lett.* **852**, L29 (2018), [arXiv:1711.03647 \[astro-ph.HE\]](#).
- [8] L. Rezzolla, E. R. Most, and L. R. Weih, Using Gravitational-wave Observations and Quasi-universal Relations to Constrain the Maximum Mass of Neutron Stars, *Astrophys. J. Lett.* **852**, L25 (2018), [arXiv:1711.00314 \[astro-ph.HE\]](#).
- [9] M. Ruiz, S. L. Shapiro, and A. Tsokaros, GW170817, general relativistic magnetohydrodynamic simulations, and the neutron star maximum mass, *Phys. Rev. D* **97**, 021501 (2018), [arXiv:1711.00473 \[astro-ph.HE\]](#).
- [10] E. R. Most, L. R. Weih, L. Rezzolla, and J. Schaffner-Bielich, New Constraints on Radii and Tidal Deformabilities of Neutron Stars from GW170817, *Phys. Rev. Lett.* **120**, 261103 (2018), [arXiv:1803.00549 \[gr-qc\]](#).
- [11] M. Shibata, E. Zhou, K. Kiuchi, and S. Fujibayashi, Constraint on the maximum mass of neutron stars using GW170817 event, *Phys. Rev. D* **100**, 023015 (2019), [arXiv:1905.03656 \[astro-ph.HE\]](#).
- [12] E. Annala, T. Gorda, A. Kurkela, J. Nättilä, and A. Vuorinen, Evidence for quark-matter cores in massive neutron stars, *Nature Physics* **16**, 907 (2020).
- [13] T. Dietrich, M. W. Coughlin, P. T. H. Pang, M. Bulla, J. Heinzl, L. Issa, I. Tews, and S. Antier, Multimessenger constraints on the neutron-star equation of state and the Hubble constant, *Science* **370**, 1450 (2020), [arXiv:2002.11355 \[astro-ph.HE\]](#).
- [14] A. Nathanail, E. R. Most, and L. Rezzolla, GW170817 and GW190814: Tension on the Maximum Mass, *Astrophys. J. Lett.* **908**, L28 (2021), [arXiv:2101.01735 \[astro-ph.HE\]](#).
- [15] N. Stergioulas, A. Bauswein, K. Zagkouris, and H.-T. Janka, Gravitational waves and non-axisymmetric oscillation modes in mergers of compact object binaries, *Mon. Not. R. Astron. Soc.* **418**, 427 (2011), [arXiv:1105.0368 \[gr-qc\]](#).
- [16] A. Bauswein and H.-T. Janka, Measuring Neutron-Star Properties via Gravitational Waves from Neutron-Star Mergers, *Phys. Rev. Lett.* **108**, 011101 (2012), [arXiv:1106.1616 \[astro-ph.SR\]](#).
- [17] K. Takami, L. Rezzolla, and L. Baiotti, Constraining the Equation of State of Neutron Stars from Binary Mergers, *Phys. Rev. Lett.* **113**, 091104 (2014), [arXiv:1403.5672 \[gr-qc\]](#).
- [18] S. Bernuzzi, T. Dietrich, and A. Nagar, Modeling the Complete Gravitational Wave Spectrum of Neutron Star Mergers, *Phys. Rev. Lett.* **115**, 091101 (2015), [arXiv:1504.01764 \[gr-qc\]](#).
- [19] L. Rezzolla and K. Takami, Gravitational-wave signal from binary neutron stars: A systematic analysis of the spectral properties, *Phys. Rev. D* **93**, 124051 (2016), [arXiv:1604.00246 \[gr-qc\]](#).
- [20] M. Breschi, S. Bernuzzi, D. Godzieba, A. Perego, and D. Radice, Constraints on the Maximum Densities of Neutron Stars from Postmerger Gravitational Waves with Third-Generation Observations, *Phys. Rev. Lett.* **128**, 161102 (2022), [arXiv:2110.06957 \[gr-qc\]](#).
- [21] E. R. Most, L. J. Papenfort, V. Dexheimer, M. Hanauske, S. Schramm, H. Stöcker, and L. Rezzolla, Signatures of Quark-Hadron Phase Transitions in General-Relativistic Neutron-Star Mergers, *Phys. Rev. Lett.* **122**, 061101 (2019), [arXiv:1807.03684 \[astro-ph.HE\]](#).
- [22] E. R. Most, L. Jens Papenfort, V. Dexheimer, M. Hanauske, H. Stoecker, and L. Rezzolla, On the deconfinement phase transition in neutron-star mergers, *European Physical Journal A* **56**, 59 (2020), [arXiv:1910.13893 \[astro-ph.HE\]](#).
- [23] L. R. Weih, M. Hanauske, and L. Rezzolla, Postmerger Gravitational-Wave Signatures of Phase Transitions in Binary Mergers, *Phys. Rev. Lett.* **124**, 171103 (2020), [arXiv:1912.09340 \[gr-qc\]](#).
- [24] S. Tootle, C. Ecker, K. Topolski, T. Demircik, M. Järvinen, and L. Rezzolla, Quark formation and phenomenology in binary neutron-star mergers using V-QCD, *SciPost Phys.* **13**, 109 (2022), [arXiv:2205.05691 \[astro-ph.HE\]](#).
- [25] A. Bauswein, N.-U. F. Bastian, D. B. Blaschke, K. Chatziioannou, J. A. Clark, T. Fischer, and M. Oertel, Identifying a First-Order Phase Transition in Neutron-Star Mergers through Gravitational Waves, *Phys. Rev. Lett.* **122**, 061102 (2019), [arXiv:1809.01116 \[astro-ph.HE\]](#).
- [26] S. Blacker, N.-U. F. Bastian, A. Bauswein, D. B. Blaschke, T. Fischer, M. Oertel, T. Soultanis, and S. Typel, Constraining the onset density of the hadron-quark phase transition with gravitational-wave observations, *Phys. Rev. D* **102**, 123023 (2020), [arXiv:2006.03789 \[astro-ph.HE\]](#).
- [27] S. L. Liebling, C. Palenzuela, and L. Lehner, Effects of high density phase transitions on neutron star dynamics, *Classical and Quantum Gravity* **38**, 115007 (2021), [arXiv:2010.12567 \[gr-qc\]](#).
- [28] A. Prakash, D. Radice, D. Logoteta, A. Perego, V. Nedora, I. Bombaci, R. Kashyap, S. Bernuzzi, and A. Endrizzi, Signatures of deconfined quark phases in binary neutron star mergers, *Phys. Rev. D* **104**, 083029 (2021), [arXiv:2106.07885 \[astro-ph.HE\]](#).
- [29] Y. Fujimoto, K. Fukushima, K. Hotokezaka, and K. Kyutoku, Gravitational Wave Signal for Quark Matter with Realistic Phase Transition, *Phys. Rev. Lett.* **130**, 091404 (2023), [arXiv:2205.03882 \[astro-ph.HE\]](#).
- [30] M. Ujevic, H. Gieg, F. Schianchi, S. V. Chaurasia, I. Tews, and T. Dietrich, Reverse phase transitions in binary neutron-

- star systems with exotic-matter cores, *Phys. Rev. D* **107**, 024025 (2023).
- [31] M. G. Alford, S. Mahmoodifar, and K. Schwenzer, Large amplitude behavior of the bulk viscosity of dense matter, *J. Phys.* **G37**, 125202 (2010), [arXiv:1005.3769 \[nucl-th\]](#).
- [32] M. G. Alford, L. Bovard, M. Hanauske, L. Rezzolla, and K. Schwenzer, Viscous dissipation and heat conduction in binary neutron-star mergers, *Phys. Rev. Lett.* **120**, 041101 (2018), [1707.09475 \[gr-qc\]](#).
- [33] M. G. Alford and S. P. Harris, Beta equilibrium in neutron star mergers, *Phys. Rev. C* **98**, 065806 (2018), [arXiv:1803.00662 \[nucl-th\]](#).
- [34] M. G. Alford, A. Haber, S. P. Harris, and Z. Zhang, Beta Equilibrium Under Neutron Star Merger Conditions, *Universe* **7**, 399 (2021), [arXiv:2108.03324 \[nucl-th\]](#).
- [35] P. Hammond, I. Hawke, and N. Andersson, Thermal aspects of neutron star mergers, *Phys. Rev. D* **104**, 103006 (2021), [arXiv:2108.08649 \[astro-ph.HE\]](#).
- [36] T. Celora, I. Hawke, P. C. Hammond, N. Andersson, and G. L. Comer, Formulating bulk viscosity for neutron star simulations, *Phys. Rev. D* **105**, 103016 (2022), [arXiv:2202.01576 \[astro-ph.HE\]](#).
- [37] E. R. Most, S. P. Harris, C. Plumberg, M. G. Alford, J. Noronha, J. Noronha-Hostler, F. Pretorius, H. Witek, and N. Yunes, Projecting the likely importance of weak-interaction-driven bulk viscosity in neutron star mergers, *Mon. Not. R. Astron. Soc.* **509**, 1096 (2022), [arXiv:2107.05094 \[astro-ph.HE\]](#).
- [38] S. Ghosh, B. Keshari Pradhan, and D. Chatterjee, Tidal heating as a direct probe of Strangeness inside Neutron stars, [arXiv e-prints](#), [arXiv:2306.14737 \(2023\)](#), [arXiv:2306.14737 \[gr-qc\]](#).
- [39] J. L. Ripley, R. Abhishek Hegade K., and N. Yunes, Probing internal dissipative processes of neutron stars with gravitational waves during the inspiral of neutron star binaries, *Phys. Rev. D* **108**, 103037 (2023), [arXiv:2306.15633 \[gr-qc\]](#).
- [40] L. Baiotti and L. Rezzolla, Binary neutron-star mergers: a review of Einstein's richest laboratory, *Rept. Prog. Phys.* **80**, 096901 (2017), [arXiv:1607.03540 \[gr-qc\]](#).
- [41] M. Alford, A. Harutyunyan, and A. Sedrakian, Bulk Viscous Damping of Density Oscillations in Neutron Star Mergers, *Particles*, [arXiv:2006.07975 \(2020\)](#), [arXiv:2006.07975 \[nucl-th\]](#).
- [42] M. Alford, A. Harutyunyan, and A. Sedrakian, Bulk Viscosity of Relativistic $npe\mu$ Matter in Neutron-Star Mergers, *Particles* **5**, 361 (2022), [arXiv:2209.04717 \[astro-ph.HE\]](#).
- [43] P. Hammond, I. Hawke, and N. Andersson, Impact of nuclear reactions on gravitational waves from neutron star mergers, *Phys. Rev. D* **107**, 043023 (2023).
- [44] E. R. Most, A. Haber, S. P. Harris, Z. Zhang, M. G. Alford, and J. Noronha, Emergence of Microphysical Bulk Viscosity in Binary Neutron Star Postmerger Dynamics, *Astrophys. J. Lett.* **967**, L14 (2024), [arXiv:2207.00442 \[astro-ph.HE\]](#).
- [45] D. Radice, S. Bernuzzi, A. Perego, and R. Haas, A new moment-based general-relativistic neutrino-radiation transport code: Methods and first applications to neutron star mergers, *Mon. Not. Roy. Astron. Soc.* **512**, 1499 (2022), [arXiv:2111.14858 \[astro-ph.HE\]](#).
- [46] P. L. Espino, P. Hammond, D. Radice, S. Bernuzzi, R. Gamba, F. Zappa, L. F. L. Micchi, and A. Perego, Neutrino Trapping and Out-of-Equilibrium Effects in Binary Neutron-Star Merger Remnants, *Phys. Rev. Lett.* **132**, 211001 (2024), [arXiv:2311.00031 \[astro-ph.HE\]](#).
- [47] M. Chabanov and L. Rezzolla, Impact of bulk viscosity on the post-merger gravitational-wave signal from merging neutron stars, [arXiv e-prints](#), [arXiv:2307.10464 \(2023\)](#), [arXiv:2307.10464 \[gr-qc\]](#).
- [48] I. Mueller, Zum Paradoxon der Wärmeleitungstheorie, *Zeitschrift für Physik* **198**, 329 (1967).
- [49] W. Israel, Nonstationary irreversible thermodynamics: A causal relativistic theory, *Annals of Physics* **100**, 310 (1976).
- [50] W. Israel and J. M. Stewart, Transient relativistic thermodynamics and kinetic theory, *Annals of Physics* **118**, 341 (1979).
- [51] W. A. Hiscock and L. Lindblom, Stability and causality in dissipative relativistic fluids., *Annals of Physics* **151**, 466 (1983).
- [52] L. Rezzolla and O. Zanotti, *Relativistic Hydrodynamics* (Oxford University Press, 2013).
- [53] L. Gavassino, M. Antonelli, and B. Haskell, Bulk viscosity in relativistic fluids: from thermodynamics to hydrodynamics, *Classical and Quantum Gravity* **38**, 075001 (2021), [arXiv:2003.04609 \[gr-qc\]](#).
- [54] E. R. Most and J. Noronha, Dissipative magnetohydrodynamics for nonresistive relativistic plasmas: An implicit second-order flux-conservative formulation with stiff relaxation, *Phys. Rev. D* **104**, 103028 (2021), [arXiv:2109.02796 \[astro-ph.HE\]](#).
- [55] G. Camelio, L. Gavassino, M. Antonelli, S. Bernuzzi, and B. Haskell, Simulating bulk viscosity in neutron stars. I. Formalism, *Phys. Rev. D* **107**, 103031 (2023), [arXiv:2204.11809 \[gr-qc\]](#).
- [56] G. Camelio, L. Gavassino, M. Antonelli, S. Bernuzzi, and B. Haskell, Simulating bulk viscosity in neutron stars. II. Evolution in spherical symmetry, *Phys. Rev. D* **107**, 103032 (2023), [arXiv:2204.11810 \[gr-qc\]](#).
- [57] M. D. Duez, Y. T. Liu, S. L. Shapiro, and B. C. Stephens, General relativistic hydrodynamics with viscosity: Contraction, catastrophic collapse, and disk formation in hypermassive neutron stars, *Phys. Rev. D* **69**, 104030 (2004), [astro-ph/0402502](#).
- [58] D. Radice, General-relativistic Large-eddy Simulations of Binary Neutron Star Mergers, *Astrophys. J. Lett.* **838**, L2 (2017), [arXiv:1703.02046 \[astro-ph.HE\]](#).
- [59] M. Shibata, K. Kiuchi, and Y.-i. Sekiguchi, General relativistic viscous hydrodynamics of differentially rotating neutron stars, *Phys. Rev. D* **95**, 083005 (2017).
- [60] M. Shibata and K. Kiuchi, Gravitational waves from remnant massive neutron stars of binary neutron star merger: Viscous hydrodynamics effects, *Phys. Rev. D* **95**, 123003 (2017), [arXiv:1705.06142 \[astro-ph.HE\]](#).
- [61] M. D. Duez, A. Knight, F. Foucart, M. Haddadi, J. Jesse, F. Hébert, L. E. Kidder, H. P. Pfeiffer, and M. A. Scheel, Comparison of momentum transport models for numerical relativity, *Phys. Rev. D* **102**, 104050 (2020), [arXiv:2008.05019 \[gr-qc\]](#).
- [62] Y. Yang, M. Hippert, E. Speranza, and J. Noronha, Far-from-equilibrium bulk-viscous transport coefficients in neutron star mergers, *Phys. Rev. C* **109**, 015805 (2024), [arXiv:2309.01864 \[nucl-th\]](#).
- [63] M. G. Alford and S. P. Harris, β equilibrium in neutron-star mergers, *Phys. Rev. C* **98**, 065806 (2018), [arXiv:1803.00662 \[nucl-th\]](#).
- [64] R. F. Sawyer, Bulk viscosity of hot neutron-star matter and the maximum rotation rates of neutron stars, *Phys. Rev. D* **39**, 3804 (1989).
- [65] M. M. Disconzi, T. W. Kephart, and R. J. Scherrer, On a viable first-order formulation of relativistic viscous fluids and its applications to cosmology, *International Journal of Modern Physics D* **26**, 1750146 (2017), [https://doi.org/10.1142/S0218271817501462](#).
- [66] F. S. Bemfica, M. M. Disconzi, and J. Noronha, Nonlinear causality of general first-order relativistic viscous hydrodynamics, *Phys. Rev. D* **100**, 104020 (2019).
- [67] P. Kovtun, First-order relativistic hydrodynamics is stable, *Journal of High Energy Physics* **2019**, 34 (2019).

- [68] R. E. Houtt and P. Kovtun, Stable and causal relativistic Navier-Stokes equations, *Journal of High Energy Physics* **2020**, 67 (2020), [arXiv:2004.04102 \[hep-th\]](#).
- [69] F. Taghinavaz, Causality and Stability Conditions of a Conformal Charged Fluid, *JHEP* **08**, 119, [arXiv:2004.01897 \[hep-th\]](#).
- [70] A. Pandya, E. R. Most, and F. Pretorius, Causal, stable first-order viscous relativistic hydrodynamics with ideal gas microphysics, *Phys. Rev. D* **106**, 123036 (2022), [arXiv:2209.09265 \[gr-qc\]](#).
- [71] H. Bantilan, Y. Bea, and P. Figueras, Evolutions in first-order viscous hydrodynamics, *Journal of High Energy Physics* **2022**, 298 (2022), [arXiv:2201.13359 \[hep-th\]](#).
- [72] M. Chabanov, L. Rezzolla, and D. H. Rischke, General-relativistic hydrodynamics of non-perfect fluids: 3+1 conservative formulation and application to viscous black hole accretion, *Mon. Not. R. Astron. Soc.* **505**, 5910 (2021), [arXiv:2102.10419 \[gr-qc\]](#).
- [73] M. Alcubierre, *Introduction to 3 + 1 Numerical Relativity* (Oxford University Press, Oxford, UK, 2008).
- [74] L. Gavassino and J. Noronha, Relativistic bulk-viscous dynamics far from equilibrium, *arXiv e-prints*, [arXiv:2305.04119 \(2023\)](#), [arXiv:2305.04119 \[gr-qc\]](#).
- [75] G. S. Denicol, H. Niemi, E. Molnár, and D. H. Rischke, Derivation of transient relativistic fluid dynamics from the boltzmann equation, *Phys. Rev. D* **85**, 114047 (2012).
- [76] E. R. Most, L. J. Papenfort, and L. Rezzolla, Beyond second-order convergence in simulations of magnetized binary neutron stars with realistic microphysics, *Mon. Not. R. Astron. Soc.* **490**, 3588 (2019), [arXiv:1907.10328 \[astro-ph.HE\]](#).
- [77] S. Bernuzzi and D. Hilditch, Constraint violation in free evolution schemes: comparing BSSNOK with a conformal decomposition of Z4, *Phys. Rev. D* **81**, 084003 (2010), [arXiv:0912.2920 \[gr-qc\]](#).
- [78] D. Alic, C. Bona-Casas, C. Bona, L. Rezzolla, and C. Palenzuela, Conformal and covariant formulation of the Z4 system with constraint-violation damping, *Phys. Rev. D* **85**, 064040 (2012), [arXiv:1106.2254 \[gr-qc\]](#).
- [79] L. Del Zanna, O. Zanotti, N. Bucciantini, and P. Londrillo, ECHO: a Eulerian conservative high-order scheme for general relativistic magnetohydrodynamics and magnetodynamics, *Astron. Astrophys.* **473**, 11 (2007), [arXiv:0704.3206](#).
- [80] Z. B. Etienne, V. Paschalidis, R. Haas, P. Mösta, and S. L. Shapiro, IllinoisGRMHD: an open-source, user-friendly GRMHD code for dynamical spacetimes, *Class. Quantum Grav.* **32**, 175009 (2015), [arXiv:1501.07276 \[astro-ph.HE\]](#).
- [81] F. Galeazzi, W. Kastaun, L. Rezzolla, and J. A. Font, Implementation of a simplified approach to radiative transfer in general relativity, *Phys. Rev. D* **88**, 064009 (2013), [arXiv:1306.4953 \[gr-qc\]](#).
- [82] F. S. Bemfica, M. M. Disconzi, and J. Noronha, Causality of the einstein-israel-stewart theory with bulk viscosity, *Phys. Rev. Lett.* **122**, 221602 (2019).
- [83] P. Cerdá-Durán, Numerical viscosity in hydrodynamics simulations in general relativity, *Classical and Quantum Gravity* **27**, 205012 (2010), [arXiv:0912.1774 \[astro-ph.SR\]](#).
- [84] J. A. Font, T. Goodale, S. Iyer, M. Miller, L. Rezzolla, E. Seidel, N. Stergioulas, W.-M. Suen, and M. Tobias, Three-dimensional numerical general relativistic hydrodynamics. II. Long-term dynamics of single relativistic stars, *Phys. Rev. D* **65**, 084024 (2002), [gr-qc/0110047](#).
- [85] D. Radice and L. Rezzolla, THC: a new high-order finite-difference high-resolution shock-capturing code for special-relativistic hydrodynamics, *Astron. Astrophys.* **547**, A26 (2012), [arXiv:1206.6502 \[astro-ph.IM\]](#).
- [86] D. Radice, L. Rezzolla, and F. Galeazzi, Beyond second-order convergence in simulations of binary neutron stars in full general-relativity, *Mon. Not. R. Astron. Soc. L.* **437**, L46 (2014), [arXiv:1306.6052 \[gr-qc\]](#).
- [87] F. Löffler, J. Faber, E. Bentivegna, T. Bode, P. Diener, R. Haas, I. Hinder, B. C. Mundim, C. D. Ott, E. Schnetter, G. Allen, M. Campanelli, and P. Laguna, The Einstein Toolkit: A Community Computational Infrastructure for Relativistic Astrophysics, *Class. Quantum Grav.* **29**, 115001 (2012), [arXiv:1111.3344 \[gr-qc\]](#).
- [88] H. Togashi, K. Nakazato, Y. Takehara, S. Yamamuro, H. Suzuki, and M. Takano, Nuclear equation of state for core-collapse supernova simulations with realistic nuclear forces, *Nucl. Phys. A* **961**, 78 (2017), [arXiv:1702.05324 \[nucl-th\]](#).
- [89] A. Figura, J. J. Lu, G. F. Burgio, Z. H. Li, and H. J. Schulze, Hybrid equation of state approach in binary neutron-star merger simulations, *Phys. Rev. D* **102**, 043006 (2020), [arXiv:2005.08691 \[gr-qc\]](#).
- [90] M. Hanauske, K. Takami, L. Bovard, L. Rezzolla, J. A. Font, F. Galeazzi, and H. Stöcker, Rotational properties of hypermassive neutron stars from binary mergers, *Phys. Rev. D* **96**, 043004 (2017), [arXiv:1611.07152 \[gr-qc\]](#).
- [91] S. Fujibayashi, K. Kiuchi, S. Wanajo, K. Kyutoku, Y. Sekiguchi, and M. Shibata, Comprehensive Study of Mass Ejection and Nucleosynthesis in Binary Neutron Star Mergers Leaving Short-lived Massive Neutron Stars, *Astrophys. J.* **942**, 39 (2023), [arXiv:2205.05557 \[astro-ph.HE\]](#).
- [92] M. Shibata and K. Hotokezaka, Merger and mass ejection of neutron star binaries, *Annual Review of Nuclear and Particle Science* **69**, 41 (2019), <https://doi.org/10.1146/annurev-nucl-101918-023625>.
- [93] A. Schmitt and P. Shternin, Reaction Rates and Transport in Neutron Stars, in *Astrophysics and Space Science Library*, Astrophysics and Space Science Library, Vol. 457, edited by L. Rezzolla, P. Pizzochero, D. I. Jones, N. Rea, and I. Vidaña (2018) p. 455, [arXiv:1711.06520 \[astro-ph.HE\]](#).
- [94] C. Cutler, L. Lindblom, and R. J. Splinter, Damping Times for Neutron Star Oscillations, *ApJ* **363**, 603 (1990).
- [95] L. Baiotti, R. De Pietri, G. M. Manca, and L. Rezzolla, Accurate simulations of the dynamical bar-mode instability in full general relativity, *Phys. Rev. D* **75**, 044023 (2007), [astro-ph/0609473](#).
- [96] K. Takami, L. Rezzolla, and L. Baiotti, Spectral properties of the post-merger gravitational-wave signal from binary neutron stars, *Phys. Rev. D* **91**, 064001 (2015), [arXiv:1412.3240 \[gr-qc\]](#).